RESEARCH

Using musculoskeletal models to generate physically-consistent data for 3D human pose, kinematic, dynamic, and muscle estimation

Ali Nasr[1] · Kevin Zhu[1] · John McPhee[1]

Abstract
Human motion capture technology is utilized in many industries, including entertainment, sports, medicine, augmented reality, virtual reality, and robotics. However, motion capture data only allows the user to analyze human movement at a kinematic level. In order to study the corresponding dynamics and muscle properties, additional sensors such as force plates and electromyography sensors are needed to collect the relevant data. Collecting, processing, and synchronizing data from multiple sources could be laborious and time-consuming. This study proposes a method to generate the dynamics and muscle properties of existing motion capture datasets. To do so, our method reconstructs motions via kinematics, dynamics, and muscle modeling with a musculoskeletal model consisting of 14 joints, 40 degrees of freedom, and 15 segments. Compared to current physics simulators, our method also infers muscle properties to ensure our human model is realistic. We have met International Society of Biomechanics standards for all terminologies and representations. Furthermore, our integrated musculoskeletal model allows the user to preselect various anthropometric features of the human performing the motion, such as height, mass, level of athleticism, handedness, and skin temperature, which are often infeasible to estimate from monocular videos without appropriate annotations. We apply our method on the Human3.6M dataset and show that our reconstructed motion is kinematically similar to the ground truth markers while being dynamically plausible when compared to experimental data found in literature. The generated data (Human3.6M+) is available for download.

1 Introduction

Human motion capture technology is used in many applications, such as character animation in video games and movies, biomechanical analysis in sports and medicine, and human–computer interaction in robotics. Traditional motion capture systems necessitate the use

---

✉ A. Nasr
   a.nasr@uwaterloo.ca

1   Department of Systems Design Engineering, University of Waterloo, Waterloo, ON, Canada
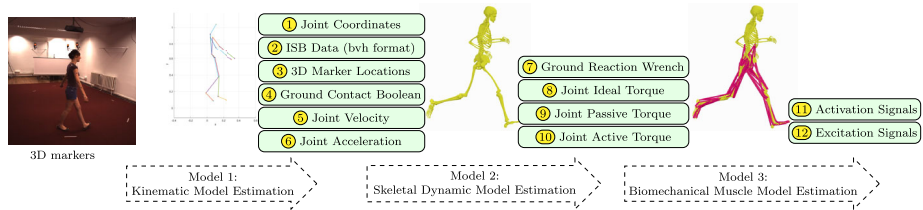
Fig. 1 Serial utilization of the input 3D markers, as well as the target kinematic, skeletal dynamic, and biomechanical muscle data, which could be used for training machine learning models

of marker suits, as outlined by Menache [1], which pose financial, physical, and usability constraints. In response, researchers have developed marker-less motion capture technology as a more accessible alternative.

Three-dimensional human pose estimation (HPE) is an active research area in computer vision pertaining to the retrieval of 3D human joint positions from images. The two main approaches are direct estimation of 3D keypoints from images [2–4] and lifting 2D keypoints to 3D [5–7]. A subfield, model-based human pose and shape estimation (HPSE) [8, 9], estimates inputs that are fed into a parametric human model, which subsequently outputs a triangulated mesh representing the surface of a human body. The most popular human parametric model, the skinned multi-person linear (SMPL) model [10], uses a collection of linear functions to map rotation- and shape-based parameters to a triangulated mesh of 6890 vertices. SMPL is also the first parametric human model to be compatible with game engines. However, since many 3D pose estimators are purely data-driven, the human structural information is modeled implicitly, and the outputs may contain anatomically impossible human poses (e.g., inverted joints, inconsistent skeleton sizes) or physically impossible movements (e.g., floating, ground penetration, excessive leaning). For many studies that rely on the biomechanical analysis of motion capture data, these artifacts render their results unreliable or unusable.

To estimate more plausible motions, recent optimization-based pose estimators [11–13] reconstruct the initial data-driven estimations using external physics simulators to enforce the laws of physics. Regression-based methods [14, 15], on the other hand, use neural networks to directly evaluate forces and torques as auxiliary estimates and incorporate dynamic equations into the loss function. However, due to the lack of large-scale force-annotated motion capture video datasets, the estimated forces and torques are not directly supervised and physical plausibility could be sacrificed to optimize 3D joint positional accuracy.

Motivated by this data deficiency, we propose to generate the dynamics and muscle properties of human motions in existing motion capture datasets, allowing for better training and validation data for physics-based deep learning models (Fig. 1). Moreover, current optimization-based pose estimators often rely on general-purpose physics simulators [16, 17] and unrealistic human body models consisting of rigid 3D shape primitives, which limit the plausibility of the output motions, as described in [18]; these human models are also significantly different from the parametric human models [10] used for HPSE. To address these plausibility concerns, we propose to integrate human musculoskeletal modeling into our optimization scheme to produce more realistic human motions [19]. This further allows for the inference of muscle properties, which are unavailable from the aforementioned physics simulators. In addition, we ensure our human model is realistic by meeting International Society of Biomechanics (ISB) standards, which conveniently results in poses similar to the SMPL skeleton, making our generated data compatible with many existing

HPSE frameworks. As a proof of concept, we use our method to generate the dynamics and muscle properties of the motions in the Human3.6M dataset [20]. The generated data is available for download on GitHub[1] and on our website.[2]

In summary,

1. We develop a novel motion reconstruction method to generate realistic human dynamics and muscle properties by incorporating musculoskeletal modeling and ISB standards.
2. Compared to previous physics simulators, the inclusion of muscle modeling allows us to infer muscle signals.
3. Our human model (consisting of 14 joints, 40 degrees of freedom (DoFs), and 15 segments), constrained by ISB standards, is similar to the SMPL skeleton.
4. We apply and evaluate our method on the Human3.6M dataset. The results and code are made available for research, allowing users to access the generated dynamics and muscle properties associated with the motions in the Human3.6M dataset to train physics-based deep learning models.

The remainder of this manuscript is outlined as follows. Section 2 describes the structures of our input and generated data. Section 3 describes our skeletal dynamic model built to ISB standards. Sections 4–6 detail the kinematic, dynamic, and muscle modeling steps of our method. Finally, we evaluate and discuss our results in Sect. 7.

2 Data

2.1 Raw input 3D markers database

As a demonstration, we apply our method to the Human3.6M dataset [20], and infer the associated dynamics and muscle properties of each motion. Human3.6M is a popular indoor benchmark dataset for single-person 3D HPE, comprising over 3.6 million distinct human poses. We reconstruct the motions performed by the seven actors (Subjects 1, 5, 6, 7, 8, 9, and 11) using publicly available motion capture data.[3] The body mass indices of these actors span from 17 to 29. Each actor performs 15 actions, labeled *Directions, Discussion, Eating, Greeting, Phone Talk, Posing, Buying, Sitting, Sitting Down, Smoking, Taking Photo, Waiting, Walking, Walking the Dog,* and *Walking in Pairs*. As explicitly depicted in Fig. 2, this raw input will be utilized in Sect. 4.1 as the ground truth, represented in the form of a constructed 3D skeleton model.

2.2 Processed data structure

The synthetic database (Human3.6M+) is available for both female and male subjects, including default and dimensionless variations. This database (Human3.6M+) is provided in multiple formats, including comma-separated values, biovision hierarchy, and video files. The provided data is generated with a frame rate of 50 Hz. The id codes for markers and variables are defined in Table 1.

---

[1] https://github.com/ainlamyae/Human3.6Mplus.

[2] https://uwaterloo.ca/motion-research-group.
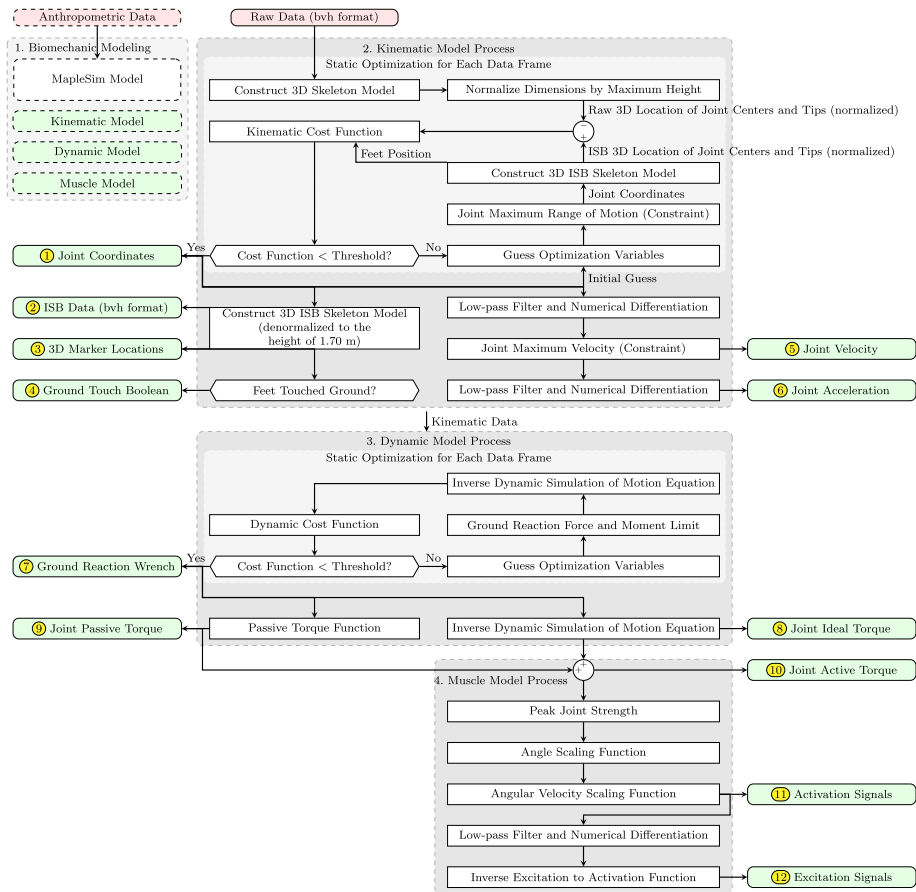
[3] http://vision.imar.ro/human3.6m.

Fig. 2 Diagram illustrating the synthetic data generation pipeline, comprising four distinct stages: 1. Biome-chanical modeling, 2. Kinematic model process, 3. Dynamic model process, and 4. Muscle model process. Output data identified by circled members

– *Subject with default anthropometrics*

The processed database includes information for a default subject with the following anthropometric characteristics: 25 years; 70 kg mass; 1.70 m height; 1 workout session per week; right-handed.

– *Subject with dimensionless data*

The positional data within this database (Human3.6M+), such as 3D marker locations or pelvis coordinate data, has undergone normalization relative to the subject's height. Concurrently, the forces have been normalized based on the subject's weight, and the torques have been normalized by the product of the subject's weight and height. The joint angles and passive torque values have remained unaltered and have not undergone any form of normalization. The output or saved data highlighted by the yellow circles in Fig. 2, and for simplicity, the aforementioned normalizations for dimensionless data are not repeated across all output data. The process of scaling this section of the database to accommodate different subject anthropometrics is a straightforward one, involving the

Table 1 ID of database markers and variables with definition of 14 joints, 5 points, 15 segments, 40 DoFs, positive and negative

Marker ID	Joint/point	Distal segment	Variable Id	DoF	Positive	Negative
K1		Pelvis	J1	PX	North	South
			J2	PY	Up	Down
			J3	PZ	West	East
			J4	PRLY	Right Yaw (+Y-axis)	Left Yaw (–Y-axis)
			J5	PRLR	Right Roll (+X-axis)	Left Roll (–X-axis)
			J6	PRLP	Right Pitch (+Z-axis)	Left Pitch (–Z-axis)
	Lumbar	Torso	J7	TFE	Extension	Flexion
			J8	TRLLF	Right Lateral Flexion	Left Lateral Flexion
			J9	TRLAR	Left Axial Rotation	Right Axial Rotation
K2	Neck	Head	J10	NFE	Extension	Flexion
			J11	NRLLF	Right Lateral Flexion	Left Lateral Flexion
			J12	NRLAR	Left Axial Rotation	Right Axial Rotation
K3	Head Vertex					
K4	Right Shoulder	Right Upper Arm	J13	RSFE	Flexion	Extension
			J14	RSAA	Adduction	Abduction
			J15	RSMLR	Medial Rotation	Lateral Rotation
K5	Right Elbow	Right Forearm	J16	REFE	Flexion	Extension
			J17	RFPS	Pronation	Supination
K6	Right Wrist	Right Hand	J18	RWFE	Flexion	Extension
			J19	RWRUD	Ulnar Deviation	Radial Deviation
K7	Right 3rd Fingertip					
K8	Left Shoulder	Left Upper Arm	J20	LSFE	Flexion	Extension
			J21	LSAA	Abduction	Adduction
			J22	LSMLR	Lateral Rotation	Medial Rotation
K9	Left Elbow	Left Forearm	J23	LEFE	Flexion	Extension
			J24	LFPS	Supination	Pronation
K10	Left Wrist	Left Hand	J25	LWFE	Flexion	Extension
			J26	LWRUD	Radial Deviation	Ulnar Deviation
K11	Left 3rd Fingertip					
K12	Right Hip	Right Thigh	J27	RHFE	Flexion	Extension
			J28	RHAA	Adduction	Abduction
			J29	RHIER	Internal Rotation	External Rotation
K13	Right Knee	Right Leg	J30	RKFE	Extension	Flexion
K14	Right Ankle	Right Foot	J31	RADPF	Dorsiflexion	Plantar Flexion
			J32	RAEI	Eversion	Inversion
			J33	RAAA	Adduction	Abduction
K15	Right 2nd Toe Tip					

Table 1 (*Continued*)

Marker ID	Joint/point	Distal segment	Variable Id	DoF	Positive	Negative
K16	Left Hip	Left Thigh	J34	LHFE	Flexion	Extension
			J35	LHAA	Abduction	Adduction
			J36	LHIER	External Rotation	Internal Rotation
K17	Left Knee	Left Leg	J37	LKFE	Extension	Flexion
K18	Left Ankle	Left Foot	J38	LADPF	Dorsiflexion	Plantar Flexion
			J39	LAEI	Inversion	Eversion
			J40	LAAA	Abduction	Adduction
K19	Left 2nd Toe Tip					

multiplication of positional data by the subject's body height, forces by the subject's weight, and torques by the product of the subject's weight and height.

3 Step 1: skeletal dynamic modeling

The data processing (Fig. 2) is accomplished by means of a comprehensive biomechanical model, which comprises two subsystems: a skeletal dynamic model and a muscle dynamic model [21]. The skeletal model is introduced in the present section, while the muscle model is presented in Sect. 5.

3.1 Locations of anatomical landmarks

The global reference frame is affixed to the ground, and subsequently, the initial segment, namely the pelvis, is endowed with 6 DoFs. The torso, consisting of a single segment, jointly represents the thorax and abdomen regions, as the precise estimation of the thoracic joint center remains a challenging task [22]. All coordinate frames adhere to the anatomical landmarks as per the ISB standards [23]; the joint centers are established in accordance with the existing literature, utilizing the designated anatomical landmarks. The orientations of the segment coordinate systems are defined as depicted in [24] and [25] for upper and lower body [22, 23]. The nomenclature and acronyms pertaining to the anatomical landmarks for each segment are adopted from [22, 23]. The anatomical coordinate systems for these segments are rigorously defined using these key landmarks and are presented in [24] and [25] for upper and lower body according to [22, 23, 26].

The placements of the centers of mass (CoMs) and anatomical markers on the right side of the body, as depicted in [24] and [25] for upper and lower body, were adopted from the raw location data of Dumas et al [22]; the resulting scaled data are presented in [24] and [25] for upper and lower body.

We presume symmetry between the right and left limbs. Consistent with the approach taken in [24], the matrix described in equation (1) serves to transpose the positions of anatomical landmarks and segment CoM from the right limb, as detailed in [24] and [25] for upper and lower body, to the corresponding positions on the left limb,

$$R_{R2L} = \begin{bmatrix} 1 & 0 & 0 \\ 0 & 1 & 0 \\ 0 & 0 & -1 \end{bmatrix}. \tag{1}$$

3.2 Body segment inertia parameters

It is customary to compute the body segment inertial parameters using established linear or nonlinear regression formulae [22, 26–28]. In [24] and [25] for upper and lower body, the mass of each segment (M) is presented as a fraction of the total body mass, as outlined in [26]. The inertia tensor is determined based on the origins of the segment coordinate axes. More specifically, akin to the approach employed in [24], equation (2) delineates the segment's inertia matrix (I) as a function of the segment length (L) and segment mass for the right limb. Scaling factors (r) for the inertia matrix, along with the scaled segment lengths relative to body height and scaled segment masses relative to body mass, are provided in [24] and [25] for upper and lower body.

Note that the segments are treated as rigid bodies. This simplifies calculations by maintaining constant segment lengths, thereby enabling a concentrated examination of joint movements without needing to address deformations or length changes.

Through the application of equation (3), which utilizes the matrix defined in equation (1), the conversion of the equivalent inertia matrix from the right limb, as expressed in equation (2), enables the computation of the segment inertia matrix for the left limb:

$$I_R = ML^2 \begin{bmatrix} r_{xx}^2 & r_{xy}^2 & r_{xz}^2 \\ r_{xy}^2 & r_{yy}^2 & r_{yz}^2 \\ r_{xz}^2 & r_{yz}^2 & r_{zz}^2 \end{bmatrix}, \tag{2}$$

$$I_L = R_{R2L}^T I_R R_{R2L}, \tag{3}$$

where

M the mass of each segment,
L the segment length,
r the scaling factors for the inertia matrix.

3.3 Degrees of freedom

The multibody kinematic model encompasses a total of 40 DoF:

– 6 DoF for pose (position and orientation) of the pelvis in 3D space.
– 3 DoF for the torso (torso flexion/extension (TFE), torso right/left lateral flexion (TRLLF), and torso right/left axial rotation (TRLAR)).
– 3 DoF for the neck (neck flexion/extension (NFE), neck right/left lateral flexion (NRLLF), and neck right/left axial rotation (NRLAR)).
– 3 DoF for each shoulder (shoulder flexion/extension (SFE), shoulder adduction/abduction (SAA), and shoulder medial/lateral rotation (SMLR)).
– 2 DoF for each elbow (elbow flexion/extension (EFE) and forearm pronation/supination (FPS)).
– 2 DoF for each wrist (wrist flexion/extension (WFE) and wrist radial/ulnar deviation (WRUD)).
– 3 DoF for each hip (hip flexion/extension (HFE), hip adduction/abduction (HAA), and hip internal/external rotation (HIER)).
– 1 DoF for each knee (knee flexion/extension (KFE)).
– 3 DoF for each ankle (ankle dorsiflexion/plantar flexion (ADPF), ankle eversion/inversion (AEI), and ankle adduction/abduction (AAA)).
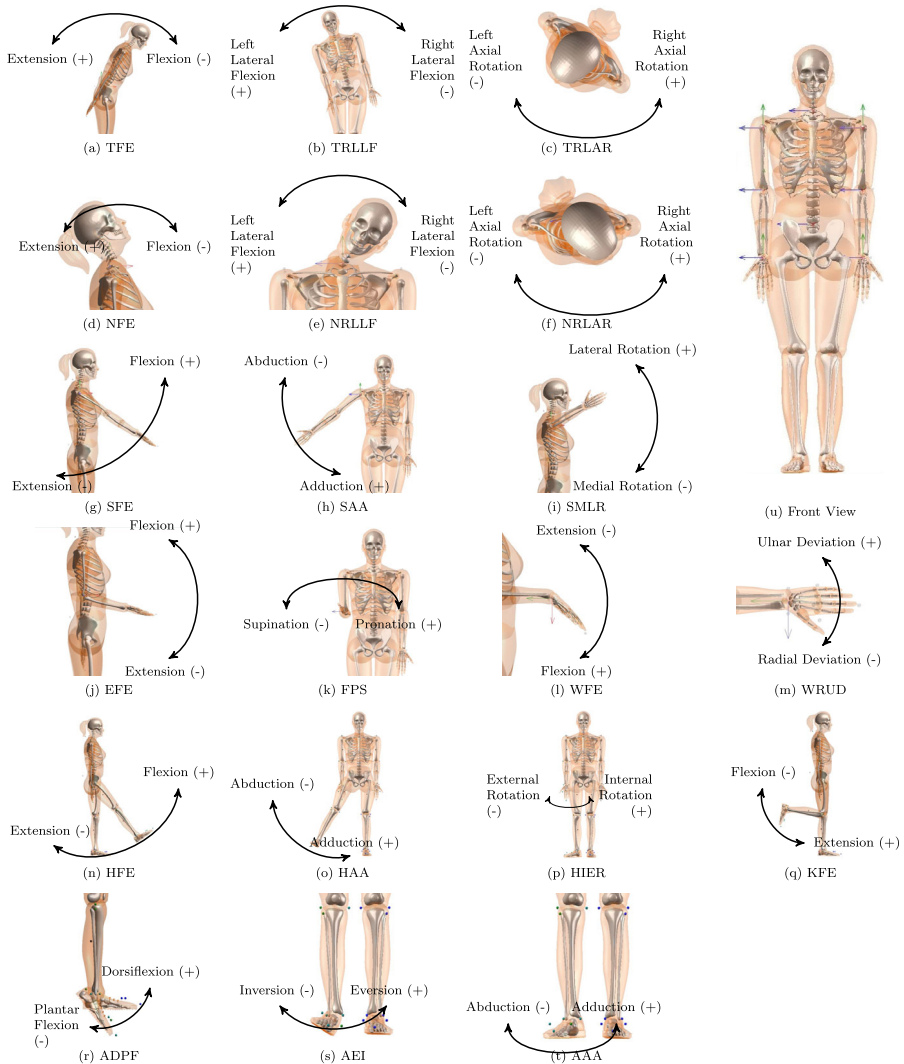
Fig. 3 Depiction of musculoskeletal model DoF and directions for (a) TFE, (b) TRLLF, (c) TRLAR, (d) NFE, (e) NRLLF, (f) NRLAR, (g) SFE, (h) SAA, (i) SMLR, (j) EFE, (k) FPS, (l) WFE, (m) WRUD, (n) HFE, (o) HAA, (p) HIER, (q) KFE, (r) ADPF, (s) AEI, (t) AAA, and (u) Front view with the initial posture (zero joint angles)

The rationale for selecting these DoFs is substantiated by their capacity to represent full-body motion, coupled with the existing biomechanical data related to these DoFs, as documented in the literature. While a greater number of DoFs would enhance the spinal modeling of the trunk and the scapular joint, the lack of biomechanical data the literature sources currently limits such expansion.

A comprehensive overview of the definitions and motion characteristics associated with DoFs, as detailed in [24] and [25] for upper and lower body (or Table 4 located in the Appendix) and visually depicted in Fig. 3. Notably, the left limb exhibits reversed directions
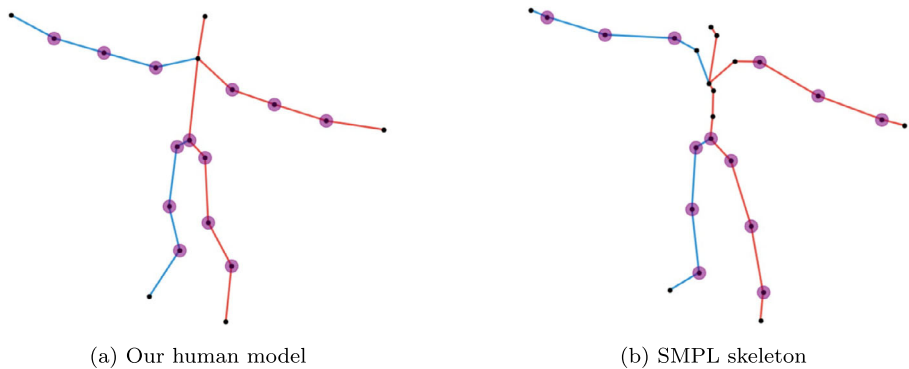
(a) Our human model   (b) SMPL skeleton

Fig. 4 (a) representing our human model and (b) showcasing the SMPL skeleton. The 13 common joints used for positional evaluation are shaded circles (purple)

for DoFs such as SAA, SMLR, FPS, WRUD, HAA, HIER, AAA, and AEI, in contrast to the information provided for the right limb in [24] and [25] for upper and lower body (or Table 4).

4 Step 2: kinematic model processing

Initially, the raw data from the aforementioned databases serves as the primary input for the kinematic processing, which is described as follows:

4.1 Joint coordinates

The raw data in biovision hierarchy format was utilized to animate a nonstandard 3D skeleton model, which is based on biovision hierarchy data. Subsequently, the dimensions of this nonstandard 3D skeleton model were normalized to the maximum height specified in the biovision hierarchy format. Following normalization, the raw 3D coordinates of joint centers and tips were compared with the corresponding ISB 3D coordinates of joint centers and tips. In following paragraph this comparison described with optimization method.

In this study, we employed an optimization methodology designed to align the positions of anatomical landmarks recommended by the ISB (Fig. 4a), including joint centers, finger-tip positions, and toe positions, with the corresponding markers from raw data (Fig. 4b). The optimization procedure minimized the cost function in equation (4) to estimate the joint coordinates. Incorporated into this optimization process was the imposition of maximum joint angle limits (equation (5)) obtained from pertinent literature, as documented in [24] and [25] for upper and lower body (or Table 4). By incorporating these constraints, we ensured that the simulated motions remained consistent with physiological expectations and well within the feasible range of motion (RoM):

$$J_\theta = \sum_n \mathbf{W}_n^T \left(P_{ISB}(\boldsymbol{\theta}) - P_{Raw} \right)^2, \tag{4}$$

$$\boldsymbol{\theta}_{\min} \leq \boldsymbol{\theta} \leq \boldsymbol{\theta}_{\max}. \tag{5}$$

The resultant joint coordinates are saved in a table, a biovision hierarchy data, and a short video format.

4.2 3D ISB marker locations

The 3D coordinates of all essential markers were recorded based on the estimated joint coordinates.

4.3 Ground touch Boolean

When the ankle joint centers and toe tips were within a specific range of the minimum vertical position (in this case, we chose 3 cm through trial and error), it was assumed that the respective feet had made contact with the ground. This contact detection flag was subsequently employed for the computation of ground reaction wrench when required.

   In the context of motion capture experiment, note that if the raw data were to have high resolution with minimal error, ground detection would occur with only a deviation in vertical position. However, due to inherent errors stemming from the resolution of cameras within the motion capture system, the repeatability of detecting foot contact with the ground is subject to a threshold that necessitates trial and error exploration. Basically, during this iterative process, our aim was to identify the vertical position corresponding to foot–ground contact throughout the entire experiment, rather than at a single moment.

4.4 Seating Boolean

When the pelvis joint approached to a specific distance (in this case, we chose 5 cm through trial and error) from the vertical height of both knee joints, while pelvis is horizontally away from knee, it was deduced that contact had been established between the pelvis and the seat. This detection flag for contact was subsequently utilized for the calculation of vertical forces exerted on the seat, as needed.

4.5 Joint speed and acceleration

Joint speed and acceleration were determined through the 1st and 2nd numerical differentiation of joint coordinates. Prior to applying numerical differentiation, a data smoothing technique involving a low-pass filter with a frequency of 10 Hz was employed. This preprocessing step aimed to mitigate high variations in the data from potential variations in the optimization process.

5 Step 3: dynamic model processing

Inverse dynamics encompasses the solution of torque-driven equations of motion, as elucidated in Sect. 5.1, by utilizing kinematic data and the physical attributes of the body. This process facilitates the calculation of the resultant forces and moments acting on specific joints [29]. The inverse dynamics model used below to compute joint torques were previously validated in [24, 25].

5.1 Ground reaction wrench

In this study, we implemented an inverse dynamic simulation methodology to ascertain the ground reaction wrench, comprising both force (F_{GRW}) and torque (τ_{GRW}) constituents. The primary objective was to estimate this wrench in a manner that minimizes the resultant

pelvis wrench ($Q_{p\times 1}$), which should be zero for this free-floating body. It is noteworthy that throughout this optimization procedure, stringent constraints were imposed to ensure that the generated force and torque values remained well within reasonable upper and lower limits. This constraint-based approach serves to establish a coherent connection between the ground and the feet. Specifically, the horizontal component of the ground reaction wrench arises due to frictional effects, while the vertical component predominantly counters the gravitational force:

$$J_{GRW} = \mathbf{W}_1^T \, (\boldsymbol{\tau}_{\textbf{Pelvis}})^2 + \mathbf{W}_2^T \, (\boldsymbol{F}_{\textbf{Pelvis}})^2, \tag{6}$$

$$\begin{aligned} \boldsymbol{\tau}_{\min} \leq \boldsymbol{\tau}_{GRW} \leq \boldsymbol{\tau}_{\max}, \\ \boldsymbol{F}_{\min} \leq \boldsymbol{F}_{GRW} \leq \boldsymbol{F}_{\max}. \end{aligned} \tag{7}$$

When a subject is seated, the foot–ground reaction wrenches are diminished to a portions of their maximum value (typically around 25% as per [30], depending on chair height), with the remaining portion being counterbalanced by the seat reaction forces.

5.2 Joint ideal torque

Considering that the chosen n generalized coordinates and generalized speeds remain independent, the governing dynamic equations for the musculoskeletal system response take the form of a set of ordinary differential equations. To efficiently implement these equations in software code, the "Multibody Dynamic Exports" and "Optimized Code Generation" modules available in MapleSim [31, 32] are employed. Equation (8) represents the dynamic. It is essential to underscore that the pelvis wrench is intricately linked to the coordinates of the pelvis within the dynamic model, as articulated in equation (8):

$$\mathbf{M}_{n\times n} \, (\boldsymbol{\theta}_{n\times 1}) \, \dot{\boldsymbol{\omega}}_{n\times 1} = \mathbf{F}_{n\times 1} \, (\boldsymbol{\omega}_{n\times 1}, \boldsymbol{\theta}_{n\times 1}) + \mathbf{Q}_{n\times 1}, \tag{8}$$

$$\mathbf{Q}_{n\times 1} = \begin{bmatrix} \mathbf{Q}_{p\times 1} \\ \mathbf{Q}_{v\times 1} \end{bmatrix}, \tag{9}$$

$$\mathbf{Q}_{p\times 1} = \begin{bmatrix} \boldsymbol{F}_{\textbf{Pelvis}} \\ \boldsymbol{\tau}_{\textbf{Pelvis}} \end{bmatrix}, \tag{10}$$

where

n	the number of independent coordinates ($n = 40$) including the $p = 6$ absolute coordinates for the pelvis with respect to ground (3 translations, 3 rotations),
p	the 6 absolute coordinates for the pelvis with respect to ground (3 translations, 3 rotations),
v	$n - p$ or the number of human joints,
$\boldsymbol{\theta}$	the column matrix of generalized coordinates,
$\boldsymbol{\omega}$	the column matrix of generalized speeds,
$\mathbf{M}$	the mass matrix,
$\mathbf{F}$	the right-hand side of the dynamic equations, which consist of Coriolis, centrifugal, and gravitational effects,
$\mathbf{Q}_{n\times 1}$	the external loads, including joint ideal torques,
$\mathbf{Q}_{p\times 1}$	the residual loads on pelvis.

5.3 Joint passive torque

When the musculature, tendons, and ligaments surrounding a joint experience stress, passive torques are generated [33]. Furthermore, in proximity to the anatomical limits of joint motion, there is a notable escalation in passive joint torques [33–35]. Typically, to replicate the effects of viscous damping and nonlinear stiffness within the joint, a double exponential function akin to equation (11) is employed [36]. This function effectively constrains the joint's position within its RoM. More specifically, it induces a substantial restoring torque when θ surpasses the defined RoM boundaries, demarcated by $\theta_{\max}^-$ and $\theta_{\max}^+$. Equation (11) incorporates a damping component to account for viscoelastic properties:

$$\tau_{\text{pasive}}(\theta, \omega) = k_1 e^{-k_2\left(\theta - \theta_{\max}^-\right)} - k_3 e^{k_4\left(\theta - \theta_{\max}^+\right)} - c\,\omega, \tag{11}$$

where

k	the passive parameters identified from analyzing experimental data and fitting the nonlinear function (range from 0.5 to 6 [37], but should be less for the weaker joints such as NRLLF, NRLAR, FPS, WFE, WRUD, HIER, AEI, and AAA),
$\theta_{\max}^-$	the maximum RoM for negative direction,
$\theta_{\max}^+$	the maximum RoM for positive direction,
c	the linear coefficient of rotational damping (0.1 N m/rad [36], same for all joints),

$\theta_{\max}$ for the SAA, SMLR, FPS, WRUD, HAA, HIER, AAA, and AEI of the left limb is the negative of the value in [24] and [25] for upper and lower body (or Table 4) (which is for right limb).

5.4 Joint active torque

By virtue of equation (12), the ideal joint torques are converted into the active torques for the human system. In essence, the activation-driven model is a synthesis of equations (9) and (12):

$$\mathbf{Q}_{v\times 1} = \left[\tau_{\text{active}} + \tau_{\text{pasive}}(\boldsymbol{\theta}, \boldsymbol{\omega})\right]_{v\times 1}, \tag{12}$$

where

τ_{active}	the net active joint torque.

The computation of positive and negative active muscle torque generator (MTG) torques involves the application of one of two distinct methodologies: static optimization (utilized in this study) and dynamic optimization. Static optimization is categorized as an inverse technique due to its reliance on time-stepping procedures to optimize MTG torques, implying that each time frame is resolved in isolation from others, as discussed in [38]. Subsequent to the determination of the positive and negative active torques, the inverse dynamic simulation can ascertain the corresponding activation signals for the MTG, both positive and negative, as discussed next.

6 Step 4: muscle model processing

Several established limitations govern the torque production capabilities of human muscles at each joint. These fundamental constraints encompass force–velocity scaling, force–length scaling, and the dynamics of muscle activation. Human muscle modeling frequently employs a 3-element Hill-type muscle–tendon unit [39]. To eliminate the need to explicitly represent muscle geometries and forces, an MTG model yields joint torques that emulate muscle performance and account for joint constraints [21, 40]. In torque-driven simulations, the MTG models supply torque values at each joint, determined by the kinematics of the corresponding joint, under the assumption of monoarticular articulation [41].

Parameters for equations (13)–(16) can be determined by fitting these functions to experimental data. Experimental data collection frequently involves the use of computerized robotic dynamometers, which find application in orthopedics and sports medicine. The human dynamometer serves as a tool for measuring the net torque and speed at an isolated joint, and it is suitable for both isometric (constant muscle length) and isokinetic (constant speed) joint conditions. The muscle activation model used below was validated using experiments in which muscles were maximally activated in isometric and isokinetic tests in [24, 25]. We assume the muscle activation level is directly proportional to the active torque.

6.1 Activation signal

The expression for human active torque (τ_{active}) as computed by the MTG model is presented in equation (13). The net active joint torque, which the biomechanical model produces, is $a\tau_\omega\tau_\theta\tau_0$. The activation signal $a(t)$, which can have a value between 0 and 1, serves as the control input to the MTG model. Each DoF, representing the axis of rotation for joints, was governed by two active components within the MTG, totaling 68 distinct products ($a\tau_\omega\tau_\theta\tau_0$), with one component dedicated to each direction of joint rotation (negative and positive) – thus, two components were allocated for each joint. It is worth noting that each active MTG component operated within defined maximum torque ranges, denoted as τ_0^+ for positive MTGs and τ_0^- for negative MTGs:

$$a^+(t)\,\tau_\omega^+(\omega)\,\tau_\theta^+(\theta)\,\tau_0^+ + a^-(t)\,\tau_\omega^-(\omega)\,\tau_\theta^-(\theta)\,\tau_0^- = \tau_{\text{active}}(t),\qquad(13)$$

where

$a(t)$ the activation signal, which is converted to the excitation signal in Sect. 6.5 and equation (17),

$\tau_\omega(\omega)$ the active-torque–angular-speed scaling function, which is illustrated in Sect. 6.4 and equation (16),

$\tau_\theta(\theta)$ the active-torque–position scaling function, which is illustrated in Sect. 6.3 and equation (15),

τ_0 the peak isometric joint torque-producing capability, which is illustrated in Sect. 6.2 and equation (14).

Muscle cocontraction refers to the simultaneous activation of agonist and antagonist muscles around a joint, which stabilizes the joint and enhances movement precision. Note that, for this simulation, we assume zero cocontraction between the positive and negative active components of MTGs [42–44].

6.2 Peak joint strength

Equation (14) encapsulates the regression model governing the mean peak isometric torque. This model incorporates diverse parameters, including sex, age, body height, body mass, physical activity level, dominant side, and skin temperature. These specific parameters, as detailed in [24] and [25] for upper and lower body (or Table 5 located in the Appendix), have been derived from an extensive literature review encompassing a substantial cohort of individuals:

$$\tau_0 = (\beta_1 + \beta_2\,s + \beta_3\,e + \beta_4\,h + \beta_5\,m)\,\left(1 - \frac{\mu}{2} + \mu\,d\right)$$
$$\times (1 + \varsigma\,w)\left[1 + \rho\,\left(10 + \frac{20\arctan\left[(T-30)\pi/20\right]}{\pi}\right)\right], \tag{14}$$

where

β_i the anthropometric and torque measurements shown in [24] and [25] for upper and lower body (or Table 5),

s the subject's sex constant (for a male is 1 and for a female is 0),

e the subject's age in year,

h the subject's height in meter,

m the subject's body mass in kilogram,

w the subject's physical activity in number of workout sessions per week,

d the subject's dominant side constant (for a dominant side is 1 and for a nondominant side is 0),

T the subject's skin temperature in degree Celsius,

μ the maximum strength difference between dominant and nondominant sides (0.09 [45, 46]),

ς the impact of exercise on maximum muscular strength (0.065 [47]),

ρ the impact of skin temperature (0.03 for each degree between 20 ° to 40 ° [48]) (unitless).

6.3 Active-torque–angle scaling function

The isometric torque within the entire RoM exhibits variability owing to the nonlinear relationship between tendon force and length. The active-torque–angle curve is described utilizing either 2nd-order or 4th-order polynomial functions [49–52]. This representation employs summation notation, as indicated in equation (15). It has been normalized relative to the peak isometric torque for each joint, resulting in a value of 1 at the optimal angle:

$$\tau_\theta\,(\theta) = \mathrm{ramp}\left(\sum_{k=1}^{o+1} q_k\theta^{k-1}\right), \tag{15}$$

where

q_k the coefficient of the polynomial,

o the order of polynomial functions.

Remember the left limb exhibits a reversal in positive and negative directions for the DoFs related to SAA, SMLR, FPS, WRUD, HAA, HIER, AAA, and AEI. In [24] and [25] for upper and lower body (or Table 4), the even-indexed coefficients q for these specific DoFs in the left limb display a reversed sign.

6.4 Active-torque–angular-speed scaling function

Muscular strength is also affected by muscular speed. Consequently, the joint angular speed (ω) plays a role in determining the active torque. Drawing from the framework proposed by [53–56], and adopting the linearized Hill-type model structure [39], we implement a rational piecewise instantaneous isokinetic torque function (equation (16)) based on joint angular speed. But it is different from the Hill-type model when $\omega < 0$ [55, 57]. It has been normalized by the maximal isometric torque of each joint, resulting in a value of 1 at zero velocity. Equation (16) utilizes a negative ω to represent motions in negative directions:

$$\tau_\omega (\omega) = \begin{cases} 0, & \omega_{\max} \leq \omega, \\ \dfrac{|\omega_{\max}| - \omega}{|\omega_{\max}| + \Gamma\omega}, & 0 < \omega < \omega_{\max}, \\ 1, & \omega = 0, \\ \dfrac{(1 - R)\,|\omega_{\max}| + S\omega R\,(\Gamma + 1)}{(1 - R)\,|\omega_{\max}| + S\omega\,(\Gamma + 1)}, & \omega < 0, \end{cases} \tag{16}$$

where

ω	the joint's instantaneous angular speed,
$|\omega_{\max}|$	the absolute value of the joint's maximum angular speed that results in no torque generation,
Γ	the shape factor affecting the curvature of the torque–velocity hyperbola concentric relationship (it is valued around 3, according to [58]),
S	the slope of eccentric to concentric phase transition (at zero angular speed) (ranges from roughly 2 [37, 55] to 3 [59]),
R	the maximum eccentric isokinetic torque (τ_0) divided by maximum isometric torque (τ_0) (ranges from 1.4 [54] to 1.5 [55]).

6.5 Excitation signal

The excitation signal serves as a representation of the state of muscle fiber recruitment [60]. The excitation-to-activation function, also called activation dynamics, introduces a delay between receiving a neural excitation signal and the generation of action potentials responsible for activating muscle fibers through electrochemical processes within the muscle tissue [60]. Essentially, the function combines the periods during which muscles are active and inactive as the MTG engages and disengages [59].

Equation (17), adapted from the Hill-type muscle model, proposes a modified form of the excitation-to-activation signal [61]. This dynamic model comprises nonlinear 1st-order differential-algebraic equations [62, 63]. The excitation signal $u(t)$ from the central nervous system undergoes transformation into the activation signal $a(t)$, representing the level of muscle activation, through this 1st-order differential-algebraic equations. When considering muscles that operate at a single joint (monoarticular muscles), the excitation signal typically ranges between 0 and 1:

$$\dot{a} = \begin{cases} \dfrac{u - a}{t_{\text{act}}\,(0.5 + 1.5a)}, & u \geq a, \\ \dfrac{(u - a)\,(0.5 + 1.5a)}{t_{\text{deact}}}, & u \leq a, \end{cases} \tag{17}$$

where

$u(t)$	the excitation signal,
$a(t)$	the activation signal,
t_{act}	the muscle activation time constants (can be calculated as 40 ms plus a quarter of their age, as indicated by Thelen [64]),
t_{deact}	the muscle deactivation time constants (assumed to be four times the value of t_{act}).

7 Discussion and results

Data generation was conducted using a PC powered by an Intel® Core™ i7-3370 CPU running at a clock speed of 3.4 GHz and equipped with 16 GB of RAM. The optimization process involved in some steps resulted in a processing duration of about 10 s per frame when utilizing a random initial guess. However, this processing time was reduced to about 1 s per frame when leveraging the initial guess from the previous frame.

7.1 Evaluation results

We apply our method on the Human3.6M dataset for a female with the default anthropometrics in Sect. 2.2. After scaling our human model to match the size of the ground truth Human3.6m data, we evaluate our generated motion in terms of positional accuracy, kinematic plausibility, and dynamic plausibility.

Note that, the results compile data from all motions performed by the seven actors, with the assumption that they possess default anthropometric characteristics (mentioned in Sect. 2.2).

7.1.1 Positional accuracy

We follow standard protocol [7] and report positional accuracy in terms of root-aligned mean per joint position error (MPJPE) in Euclidean distance. This is often referred to as "Protocol 1":

$$\text{MPJPE} = \frac{1}{N^T N^J} \sum_{t=1}^{N^T} \sum_{j=1}^{N^J} ||\hat{P}_{j,t} - P_{j,t}^{\text{Raw}}||_2, \tag{18}$$

where

$P_{j,t}^{\text{Raw}}$	the ground truth (raw) 3D position of joint j at frame t,
$\hat{P}_{j,t}$	the generated 3D joint after aligning with the ground truth in root translation,
N^T	the total number of frames,
N^J	the total number of joints.

The procrustes-aligned-MPJPE (MPJPE), or "Protocol 2", is computed after aligning the generated pose with the ground truth in translation, rotation, and scale using the Procrustes method. In columns 2–3 of Table 2, we report (in mm) the MPJPE and PA-MPJPE of the 13 common joints between our human model and the SMPL skeleton – the shoulders, elbows, wrists, pelvis, hips, knees, and ankles. Due to the inherent difference between our human

Table 2 Results of the generated motions from Human3.6M for a female with default anthropometrics

Action	MPJPE (mm)	PA-MPJPE (mm)	Vel. (m/s)	Acc. (m/s^2)	GP%	Float%	Skate%	mean GRF%	max GRF%
Directions	59.42	51.36	0.19	1.62	0.11	1.15	7.36	96.32	106.35
Discussion	56.29	47.55	0.18	1.6	4.2	2.82	8.36	79.19	108.81
Eating	56.65	45.8	0.16	1.29	7.0	10.39	2.95	80.61	107.86
Greeting	73.81	58.67	0.25	2.13	1.31	7.23	12.76	88.22	108.48
Phoning	65.14	54.32	0.15	1.32	14.24	26.1	7.12	70.08	108.37
Photo	69.85	57.91	0.19	1.47	15.82	5.76	11.31	60.07	106.85
Posing	61.08	52.22	0.19	1.61	17.82	3.99	11.18	75.44	105.48
Purchases	69.23	52.16	0.2	1.69	3.71	20.73	6.91	63.31	106.25
Sitting	54.1	45.73	0.1	0.85	–	–	–	51.68	106.42
SittingDown	71.09	61.1	0.14	1.11	–	–	–	13.39	105.33
Smoking	62.57	50.35	0.14	1.14	8.31	21.31	5.32	65.98	108.01
Waiting	49.46	43.52	0.12	1.01	2.37	3.54	5.62	91.24	107.52
WalkDog	93.08	71.79	0.34	2.96	6.7	13.88	16.12	56.75	107.97
WalkTogether	89.93	73.67	0.31	2.35	0.26	20.77	5.17	69.16	108.33
Walking	100.95	84.6	0.39	2.99	1.41	20.0	7.64	55.83	108.43
average	67.73	56.07	0.2	1.62	6.24	12.22	7.88	67.35	108.81

model and the SMPL skeleton (Fig. 4), the MPJPE for the 13 common joints of a resting T-pose is 27.8 mm. Our average MPJPE is 67.7 mm, which includes the inherent errors due to model differences.

Table 3 includes the MPJPE for each joint, along with maximum errors in brackets. We see that lower errors were obtained in relatively static activities (slower movement and smaller range of motion) and in joints closer to the pelvis, whereas higher errors are found in activities involving faster movement or larger range of motion, and in joints further away from the pelvis.

7.1.2 Kinematic plausibility

We follow [13, 65] and evaluate motion smoothness (jitter) in terms of speed (in m/s) and acceleration losses (in m/s^2) in columns 4–5 of Table 2, where

$$v_{j,t} = P_{j,t} - P_{j,t-1}, \tag{19}$$

$$\alpha_{j,t} = v_{j,t} - v_{j,t-1}, \tag{20}$$

$$\text{Vel} = \frac{1}{(N^T - 1)N^J} \sum_{t=2}^{N^T} \sum_{j=1}^{N^J} ||\hat{v}_{j,t} - v_{j,t}^{GT}||_2, \tag{21}$$

$$\text{Acc} = \frac{1}{(N^T - 2)N^J} \sum_{t=3}^{N^T} \sum_{j=1}^{N^J} ||\hat{\alpha}_{j,t} - \alpha_{j,t}^{GT}||_2. \tag{22}$$

We follow [66] and report ground penetration, floating, and foot skating for nonsitting motions in columns 6–8 of Table 2. The ground penetration rate (*GP%*) is the percentage of

Table 3 Mean per joint positional error in mm (max error in brackets) of generated motions from Human3.6M for a female with default anthropometrics. Pelvis not included since the pelvis position was aligned with the ground truth to compute errors for the other joints

	Hip	Knee	Ankle	Shoulder	Elbow	Wrist	All
Directions	11.8 (126.1)	71.7 (364.6)	54.2 (580.3)	78.3 (359.1)	72.3 (611.9)	97.9 (958.0)	64.4 (958.0)
Discussion	11.5 (113.1)	79.5 (524.4)	75.4 (1177.5)	69.8 (351.6)	59.7 (457.7)	70.0 (755.0)	61.0 (1177.5)
Eating	12.3 (77.9)	79.0 (480.7)	111.0 (832.1)	58.2 (247.7)	53.2 (497.5)	54.4 (637.6)	61.4 (832.1)
Greeting	14.1 (100.0)	82.5 (408.4)	97.2 (711.3)	85.5 (435.9)	87.8 (745.4)	112.7 (1077.1)	80.0 (1077.1)
Phoning	12.7 (167.1)	83.7 (427.4)	119.7 (661.7)	65.2 (520.2)	67.4 (529.3)	74.6 (679.1)	70.6 (679.1)
Photo	13.7 (99.9)	92.2 (536.4)	100.8 (622.9)	88.5 (439.8)	78.6 (635.9)	80.2 (836.0)	75.7 (836.0)
Posing	13.7 (167.8)	82.7 (418.5)	64.7 (791.3)	80.6 (521.2)	70.8 (770.2)	84.4 (1066.4)	66.2 (1066.4)
Purchases	12.1 (93.2)	83.9 (368.7)	120.4 (671.9)	73.9 (478.1)	76.1 (710.5)	83.6 (797.7)	75.0 (797.7)
Sitting	11.3 (64.5)	68.3 (410.7)	78.0 (551.9)	59.2 (350.3)	71.5 (446.3)	63.3 (595.2)	58.6 (595.2)
SittingDown	16.1 (104.2)	109.5 (559.6)	94.8 (683.8)	72.6 (402.6)	87.6 (575.8)	81.4 (771.3)	77.0 (771.3)
Smoking	13.0 (84.7)	90.4 (460.2)	125.2 (719.9)	55.6 (319.2)	57.9 (477.9)	64.7 (720.7)	67.8 (720.7)
Waiting	11.3 (93.0)	74.2 (429.4)	57.4 (650.2)	72.0 (597.7)	60.9 (696.5)	45.6 (707.3)	53.6 (707.3)
WalkDog	18.3 (153.8)	117.5 (642.4)	166.9 (995.0)	89.8 (528.0)	93.3 (597.7)	119.2 (930.0)	100.8 (995.0)
WalkTogether	17.2 (94.1)	124.1 (438.6)	217.8 (826.9)	69.7 (275.8)	68.7 (523.9)	87.1 (778.5)	97.4 (826.9)
Walking	21.3 (115.4)	140.9 (445.0)	255.5 (824.6)	71.2 (502.2)	77.1 (617.6)	90.1 (743.9)	109.4 (824.6)
All	13.9 (167.8)	91.7 (642.4)	115.2 (1177.5)	70.9 (597.7)	70.6 (770.2)	77.9 (1077.1)	73.4 (1177.5)

frames where a joint is more than 3 cm below the ground plane. The floating rate (*Float%*) is the percentage of frames where all joints in the feet are more than 3 cm above the ground plane. Skating is defined as when a foot moves more than 2 cm in the plane parallel to the ground while in contact with the ground. The feet skating rate (*Skate%*) is the percentage of frames where skating occurs among the frames with ground contact. Although these artifacts exist to some extent, they were not explicitly controlled for during optimization; relevant constraints could be added in future work. These resulting metrics are also sensitive to our "rough" guess of the ground plane. Future work can also incorporate better ground plane estimation or utilize datasets with ground contact annotation.

7.1.3 Dynamic plausibility

We follow [13] and report the mean and maximum net ground reaction force relative to body weight (*GRF%*) in columns 9–10 of Table 2. The net ground reaction force is computed as the sum of all ground reaction wrenches on both feet. On average, the mean *GRF%* for nonsitting motions is 72.7% of body weight, which is slightly below the experimental value for walking [67, 68], which is around 80%. This is likely correlated to the floating discussed in the previous paragraph, which could be mitigated in the future with better ground contact estimation.

The resultant pelvis wrench, which underwent minimization during the ground reaction wrench estimation (detailed in Sect. 5.1), exhibits a mean squared normalized error (MSE) of 1×10^{-3}. This value could be further reduced by adjusting the optimizer's minimum error threshold, which leads to longer processing time. However, certain scenarios arose where our assumptions could not be met. For instance, in walking scenarios, there were instances where the anticipated horizontal force exerted by the feet on the ground should have exceeded our imposed constraints to prevent human slippage. Note that our adopted constraints may not universally apply to all motion scenarios.

The dynamic model (joint torques) validated elsewhere using experimental data encompassing isometric, isokinetic, and RoM evaluations for the upper body, as documented by Nasr et al [24], and similarly for the lower body in [25] (or Table 4).

The use of a muscle model incorporating realistic human constraints offers significant advantages over simply relying on joint torque values. Such a model acknowledges the intricate interplay of factors that influence human movement. Joint torque alone cannot accurately capture the complexity of human motion, as it is constrained by some variables such as the exact joint angle, angular velocity, movement direction, timing, dominant side, sex, age, height, mass, frequency of exercise, and even body temperature. Attempting to generate motions solely based on joint torque values without considering these factors would result in unrealistic movements that humans cannot physically produce. Therefore, integrating a muscle model that accounts for these realistic constraints not only enhances the accuracy and fidelity of motion data but also lays the groundwork for more meaningful applications.

The muscle activation model used was validated using experiments in which muscles were maximally activated in isometric and isokinetic tests in [24, 25]. Moreover, we have shown in Fig. 5 the MTG activation estimates obtained from the musculoskeletal models for HFE, KFE, and ADPF with experimental surface electromyography (sEMG) data from 12 leg muscles during walking motion. The MTG activation estimates were shown against the experimental data from experimental studies by Castermans et al. [69], Wu et al. [70], and Ivanenko et al. [71]. Note that the MTG activation is generated under the assumption of zero cocontraction, whereas actual sEMG signals reveal some degree of cocontraction resulting from the simultaneous activation of multiple human muscles. Accordingly, mean sEMG signals with zero cocontraction have been incorporated in Fig. 5. In addition, while the general patterns of activation for both MTG and sEMG data showed some similarities across the gait cycle, it is important to note that the comparison is not entirely apples to apples. Despite the apparent correlation, MTG and sEMG activations are not the same; sEMG measures the electrical activity produced by muscle fibers, while MTG estimates are derived from biomechanical models based on

muscle–tendon properties and joint kinematics. Consequently, the differences in methodology and the intrinsic characteristics of each data type result in distinct activation profiles, highlighting the need for cautious interpretation when comparing these two data sources.

To elaborate, we have shown the MTG's joint activation estimates in relation to specific leg muscles to understand their functional contributions during walking. For HFE, the model's estimates are shown in Fig. 5 with the activation of muscles such as the rectus femoris, sartorius, and tensor fascia latae for flexion, and the gluteus maximus, semitendinosus, biceps femoris, and semimembranosus for extension. As is evident, the estimated MTG activation has a similar pattern to the mean sEMG signal with zero cocontraction. However, for flexion, the experimental data has a maximum at 65% of the gait cycle while the estimated MTG activation has a maximum at 50% of the gait cycle, which is the time of toe-off. This discrepancy may be due to different walking patterns, particularly the swing phase of walking in different individuals. Furthermore, for extension, the estimated MTG activation ranges from 0% to 35% and from 80% to 100% of the gait cycle. Notably, it completely overlaps with the mean sEMG signal with zero cocontraction in the second part, from 80% to 100% of the gait cycle.

When evaluating KFE, the model's joint activation was contrasted with the muscle activity of the biceps femoris, gastrocnemius (lateral and medial heads), semitendinosus, and semimembranosus for flexion, and the rectus femoris, vastus lateralis, and vastus medialis for extension. As can be seen in Fig. 5, the estimated MTG activation closely mirrors the pattern of the mean sEMG signal with zero cocontraction. Notably, for flexion, the experimental data peak occurs at 43% of the gait cycle, while the estimated MTG activation peaks at 47% of the gait cycle. For extension, both maxima coincide at 9% of the gait cycle.

For ADPF, tibialis anterior activation is depicted in Fig. 5 alongside dorsiflexion estimates, while the activation of the gastrocnemius (both heads) and soleus is contrasted with plantar flexion estimates. During plantar flexion, both mean sEMG signals with zero cocontraction and MTG activation exhibit positive values (albeit with slightly different patterns) from 0% to 53% of the gait cycle, indicating a good correspondence.

In conclusion, Fig. 5 presents MTG activation alongside sEMG signals to demonstrate the extent to which MTG joint activations replicate the patterns and timing of known muscle functions and their roles in joint movements.

7.2 Integration and utilization

Our method synthesizes dynamics and muscle signals for existing 3D human motion capture datasets, providing training and validation data (Fig. 1) for physics-based HPE, HPSE, and other computer vision models. Since video data is relatively convenient to collect and store, computer vision offers an attractive approach to estimate motion variables when lab-based measurements are inappropriate. While HPE allows us to infer the kinematics of human movement from a video, further estimating joint torques and muscle signals allows users to investigate potential relationships between the inferred skeletal kinematics, muscle dynamics, and forces. By further estimating the ground reaction wrench, users are able to investigate how individuals interact with their environment. The additional information extracted
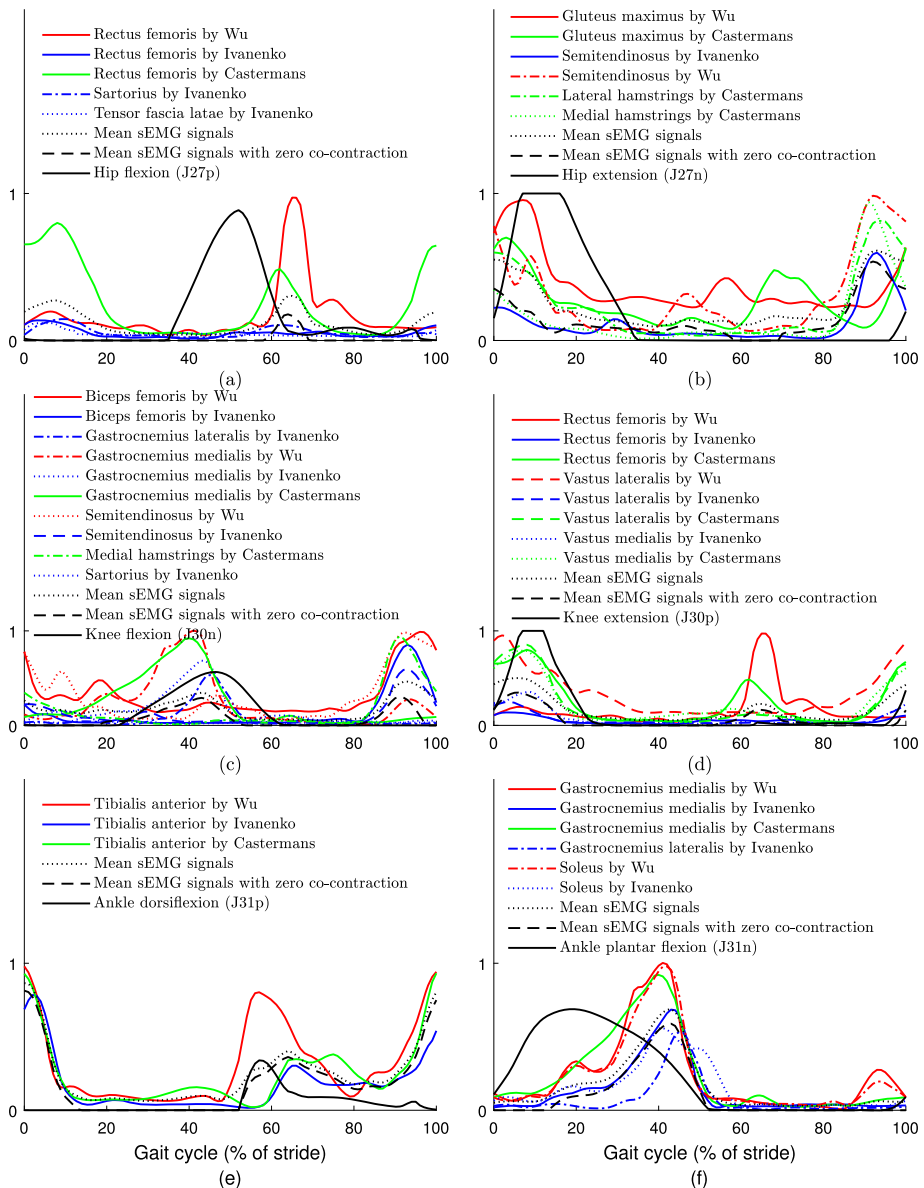
Fig. 5 The MTG activation estimates for HFE, KFE, and ADPF are highlighted with black solid lines and are compared to experimental data from Castermans et al. [69], Wu et al. [70], and Ivanenko et al. [71]. sEMG patterns from 12 leg muscles (rectus femoris, sartorius, tensor fascia latae, gluteus maximus, semitendinosus, lateral hamstrings, medial hamstrings, biceps femoris, gastrocnemius lateralis, gastrocnemius medialis, vastus lateralis, vastus medialis, tibialis anterior, and soleus) of subjects walking are shown. Mean sEMG signals with zero cocontraction have been incorporated. The MTG activation and sEMG data is provided as a percentage of the gait cycle (% of stride)

could be useful for both academic researchers and practitioners in the animation, AR/VR, medical, rehabilitation, robotics, and sports industries.

Furthermore, a multimodal approach of estimating various metrics of human movement potentially allows for more robust 3D estimations from a 2D video. Although more video datasets with force-annotations [72] or surface electromyography sensors [73] have emerged, the process of data collection, postprocessing, and synchronization from various physical sensors remains laborious and time-consuming, which limits the sample size of the collected data. Deep learning models trained on datasets with limited diversity may not generalize well in scenarios where the human's body type or performed motion is significantly different from the training data [74]. Our proposed method can increase data diversity by allowing users to generate dynamic properties from existing motion capture datasets, without having to collect new data.

7.3 Limitations

This synthetic database (Human3.6M+) for HPE, while valuable, has some limitations originating from the raw database (Human3.6M). Researchers and practitioners should be aware of these limitations when working with this HPE database and consider how these constraints might affect the accuracy, generalizability, and ethical considerations of their work.

– Limited Variability: Human3.6m contains a finite set of 3.6 million poses and movements, which may not cover the full range of real-world scenarios. This can limit the model's ability to generalize to novel or uncommon poses.
– Limited Diversity: Databases may lack diversity in terms of age, sex, body types, and clothing. This can result in bias and reduced accuracy when estimating poses for individuals who do not fit the typical profile of the database.
– Ageing and Temporal Limitations: This database (Human3.6M+) does not account for changes in human movement and posture over time, such as age-related differences or gradual changes in physical condition.
– Static Representations: This database (Human3.6M+) is typically collections of static images or frames, which may not capture accurately dynamic or temporal aspects of pose changes. Dynamic activities like sports or dance require high speed and high resolution camera recordings in addition to more specific filtering for initial data processing.
– Lack of Ground Reaction Wrench Verification: The database relies on estimated foot–ground reaction forces due to the absence of this data in the Human3.6m database. Consequently, there is a lack of verification for our estimations.

7.4 Future direction

To enhance the quality and mitigate the limitations of this HPE database, future steps should focus on several key areas. First, efforts should be directed towards diversifying input databases in terms of age, gender, body types, and clothing to ensure that the models

are more inclusive and less biased. Additionally, databases should include a more extensive range of poses, movements, and dynamic activities, acknowledging that human motion is highly variable.

The development of input databases with 3D pose and force information can provide a more accurate representation of real-world scenarios than the lacking these critical information. To increase scalability and maintain up-to-date data, collaborative efforts should be made in collecting, annotating, and sharing datasets across research communities. Undoubtedly, utilizing a force sensor between the human and the ground, or any other interaction tool, has the potential to significantly improve the precision of force and torque data.

Increasing the number of DoFs for the spine and scapula has the potential to improve the model's accuracy. However, acquiring biomechanical data for these additional DoFs from existing literature is currently unavailable. Furthermore, considering that markers in the raw dataset or from experimental motion capture systems are not fixed to the human segment and may wobble on the skin, addressing this issue could enhance the accuracy of the final processing. Note that some assumptions made in the mentioned model and computations may be disregarded by employing alternative methods, which warrant further study. Future work should incorporate contact, floating, penetration, friction, and other constraints.

These future steps will contribute to improved HPE databases, fostering more accurate, diverse, and ethical applications in a variety of domains.

8 Conclusion

Due to the limited availability of force-annotated motion capture video datasets, the estimated forces and torques of many physics-based pose estimators are not directly validated, leading to output motions that are unrealistic for humans. To address this, we generate the dynamics and muscle properties of movements from existing 3D human motion capture datasets, thus providing additional training and validation data for physics-based pose estimation. Our novel motion reconstruction method consists of a four-step approach: (1) kinematics, (2) dynamics, (3) muscle modeling, and (4) processing. Our integrated musculoskeletal model, developed from existing anthropometric and biomechanical data, allows for the inference of muscle properties, which previous physics engines do not output. We also incorporate ISB standards into our human model to increase realism. Using our method, we infer the dynamics and muscle properties of the motions in the Human3.6M dataset. We show that, kinematically, our reconstructed motion is similar to that of the SMPL skeleton fitted on the Human3.6M dataset, making our generated dynamics and muscle properties compatible with existing HPSE frameworks.

Appendix

Table 4 Abbreviations and definitions of DoF, the mean RoM for female and male, the mean peak angular velocity of the upper-body joints, and the polynomial coefficients of torque–angle scaling functions (normalized isometric torque functions)

Joint	DoF	Axis	Direction	θ_{max} (rad)			$|\omega_{max}|$ (rad/s)		Polynomial Coefficient of Torque–Angle Scaling Function in equation (15)			
				Female	Male	Ref.	Mean	Ref.	q_1	q_2	q_3	Ref.
Pelvis	X	X-axis	+ North									
			– South									
	Y	Y-axis	+ Up									
			– Down									
	Z	Z-axis	+ West									
			– East									
	Y	Y-axis	+ Right yaw									
			– Left yaw									
	X	X-axis	+ Right roll									
			– Left roll									
	Z	Z-axis	+ Right pitch									
			– Left pitch									
Torso	TFE	Z-axis	+ Extension	–0.470	–0.469	[75]	3.421	[76]	0.6093	0.7892	–0.2903	[77]
			– Flexion	0.547	0.620	[75]	2.531	[78]	0.9466	0.3969	–0.7370	[77]
	TRLLF	X-axis	+ Right Lateral Flexion	0.354	0.412	[75]	1.344	[79]	0.9995	0.0485	–1.0856	[80]
			– Left Lateral Flexion	–0.354	–0.412	[75]	1.152	[79]	0.9671	–0.4460	–1.5055	[80]
	TRLAR	Y-axis	+ Left Axial Rotation	0.730	0.868	[75]	3.176	[79]	0.9740	–0.2235	–0.4801	[80]
			– Right Axial Rotation	–0.730	–0.868	[75]	3.857	[79]	0.9903	0.1555	–0.6199	[80]
Neck	NFE	Z-axis	+ Extension	–1.288	–1.162	[81]	1.117	[82]	0.9834	0.0974	–0.1432	[83]
			– Flexion	0.972	1.004	[81]	1.134	[82]	0.7678	0.2558	–0.0337	[83]
	NRLLF	X-axis	+ Right Lateral Flexion	0.753	0.680	[81]	0.384	[84]	0.9996	0.0266	–0.3572	[24]
			– Left Lateral Flexion	–0.756	–0.770	[81]	0.384	[84]	0.9667	–0.2524	–0.4777	[24]
	NRLAR	Y-axis	+ Left Axial Rotation	1.331	1.252	[81]	0.541	[84]	0.9737	–0.0729	–0.0506	[24]
			– Right Axial Rotation	–1.360	–1.326	[81]	0.541	[84]	0.9904	0.0492	–0.0630	[24]

Table 4 (*Continued*)

Joint	DoF	Axis	Direction	$\theta_{\max}$ (rad)			$|\omega_{\max}|$ (rad/s)		Polynomial Coefficient of Torque–Angle Scaling Function in equation (15)			
				Female	Male	Ref.	Mean	Ref.	q_1	q_2	q_3	Ref.
Shoulder	SFE	Z-axis	+ Flexion	2.965	2.904	[75]	4.974	[79]	0.9992	0.0131	–0.0565	[24]
			– Extension	–1.124	–1.092	[75]	3.491	[79]	0.6621	0.3796	–0.1066	[24]
	SAA	X-axis	+ Adduction	0.199	0.283	[85]	4.084	[79]	0.8255	–0.3164	–0.1433	[24]
			– Abduction	–2.985	–2.989	[75]	4.538	[79]	0.8298	0.5322	0.1398	[24]
	SMLR	Y-axis	+ Medial Rotation	1.120	0.971	[75]	8.954	[79]	0.9390	–0.2040	–0.1702	[86]
			– Lateral Rotation	–1.571	–1.521	[75]	5.114	[79]	0.9676	–0.1777	–0.2430	[86]
Elbow	EFE	Z-axis	+ Flexion	2.402	2.344	[75]	6.231	[76]	0.4046	0.9405	–0.3714	[87]
			– Extension	0.093	0.101	[75]	4.451	[79]	0.4932	0.8047	–0.3194	[87]
	FPS	Y-axis	+ Pronation	2.859	2.774	[88]	5.184	[79]	0.7748	0.3948	–0.1731	[89]
			– Supination	–0.010	0.083	[88]	7.121	[79]	0.3414	0.7590	–0.2187	[89]
Wrist	WFE	Z-axis	+ Flexion	1.489	1.446	[75]	9.913	[90]	0.9996	0.0228	–0.3021	[87]
			– Extension	–1.391	–1.313	[75]	8.029	[79]	0.9860	0.1331	–0.3139	[87]
	WRUD	X-axis	+ Ulnar Deviation	0.281	0.284	[91]	2.740	[79]	0.9728	–0.4350	–1.7343	[92]
			– Radial Deviation	–0.401	–0.382	[91]	3.683	[79]	0.9608	–0.5288	–1.7812	[89]
Hip	HFE	Z-axis	+ Flexion	2.276	2.211	[75]	12.00	[93]	1	–0.0044	–0.1492	[94]
			– Extension	–0.281	–0.312	[75]	14.10	[93]	0.4187	0.7945	–0.2715	[94]
	HAA	X-axis	+ Adduction	0.243	0.239	[75]	2.41	[95]	0.9961	–0.2027	–2.6258	[96]
			– Abduction	–0.595	–0.560	[75]	3.14	[95]	0.8497	–1.5285	–3.8854	[96]
	HIER	Y-axis	+ Internal Rotation	0.836	0.648	[75]	4.22	[97]	0.9997	0.0392	–1.132	[98]
			– External Rotation	–0.709	–0.815	[75]	6.12	[97]	0.9998	–0.0378	–1.34	[98]
Knee	KFE	Z-axis	+ Extension	0.093	0.035	[75]	28.40	[93]	0.3385	–1.066	–0.4294	[94]
			– Flexion	–2.599	–2.567	[75]	18.60	[93]	0.5369	–0.8421	–0.3828	[94]
Ankle	ADPF	Z-axis	+ Dorsiflexion	0.417	0.389	[75]	12.70	[93]	0.9403	–0.535	–1.1989	[99]
			– Plantar Flexion	–0.944	–0.874	[75]	12.60	[93]	0.955	–0.5544	–1.7042	[99]
	AEI	X-axis	+ Eversion	0.300	0.227	[100]	2.64	[101]	0.7639	0.6787	0.3589	[99]
			– Inversion	–0.374	–0.342	[100]	6.75	[101]	0.9005	–0.6333	–1.0073	[99]
	AAA	Y-axis	+ Adduction	0.625	0.578	[100]	4.22	[97]	0.6843	–0.5254	–0.1076	[102]
			– Abduction	–0.702	–0.630	[100]	4.50	[97]	0.8808	0.315	–0.1982	[102]

Table 5 Peak joint torque for nonathletic females and males (mean of dominant and nondominant limb) and estimated parameters of peak isokinetic torque for nonathletic subjects with the anthropometric measures: body age, height, mass, and sex

Joint	DoF	Direction	Female Torque (N m)	Age (year)	Height (m)	Mass (kg)	Subject numbers	Ref.	Male Torque (N m)	Age (year)	Height (m)	Mass (kg)	Subject numbers	Ref.	β_1 (N m)	β_2 (N m)	β_3 (N m/year) Mean	Range	Ref	β_4 (N) Mean	Range	Ref	β_5 (N m/kg) Mean	Range	Ref
Torso	TFE	+	189	30	1.65	60	43	[80]	288	31	1.75	75	59	[80]	77.95	60.85	−1.6	−2.00	[103]	0.03	0.01	[104]	2.65	1.6	[105]
		−	109	30	1.65	60	43	[80]	162	31	1.75	75	59	[80]	−2.05	14.85		−1.20			0.05			3.7	
	TRLLF	+	101	30	1.65	60	43	[80]	141	31	1.75	75	59	[80]	−10.05	1.85									
		−	100	30	1.65	60	43	[80]	137	31	1.75	75	59	[80]	−11.05	−1.15									
	TRLAR	+	35	30	1.65	60	43	[80]	66	31	1.75	75	59	[80]	−76.05	−7.15									
		−	38	30	1.65	60	43	[80]	67	31	1.75	75	59	[80]	−73.05	−9.15									
Neck	NFE	+	21	30	1.64	65	5	[106]	52	32	1.77	77	11	[106]	28.41	29.95	−0.70	−1.05	[107]	0.36	0.20	[83]	0.2	0.06	[83]
		−	15	30	1.64	65	5	[106]	30	32	1.77	77	11	[106]	22.41	13.95		−0.34			0.53			0.33	
	NRLLF	+	16	30	1.64	65	5	[106]	36	32	1.77	77	11	[106]	23.41	18.95									
		−	16	30	1.64	65	5	[106]	36	32	1.77	77	11	[106]	23.41	18.95									
	NRLAR	+	6	30	1.64	65	5	[106]	15	32	1.77	77	11	[106]	13.41	7.95									
		−	6	30	1.64	65	5	[106]	15	32	1.77	77	11	[106]	13.41	7.95									
Shoulder	SFE	+	34	25	1.62	62	12	[108]	61	25	1.72	75	12	[108]	−100.95	14.83	−0.17	−0.33	[109]	71	16	[109]	0.39	0.05	[109]
		−	45	25	1.62	62	12	[108]	95	25	1.72	75	12	[108]	−89.95	37.83		−0.02			125			0.73	
	SAA	+	43	25	1.62	62	12	[108]	84	25	1.72	75	12	[108]	−91.95	28.83									
		−	23	25	1.62	62	12	[108]	46	25	1.72	75	12	[108]	−111.95	10.83									
	SMLR	+	27	25	1.62	62	12	[108]	51	25	1.72	75	12	[108]	−107.95	11.83									
		−	19	25	1.62	62	12	[108]	34	25	1.72	75	12	[108]	−115.95	2.83									
Elbow	EFE	+	33	23	1.66	67	24	[110]	63	24	1.80	81	30	[110]	−21.67	23.02	−0.12	−0.24	[109]	23.7	−6.5	[109]	0.27	0.09	[109]
		−	29	23	1.66	67	24	[110]	53	24	1.80	81	30	[110]	−25.67	17.02		−0.01			54			0.46	
	FPS	+	6.3	28	1.68	62	22	[111]	12	30	1.78	80	21	[111]	−46.90	−1.29									
		−	5.8	28	1.68	62	22	[111]	11	30	1.78	80	21	[111]	−47.40	−1.79									

Table 5 (*Continued*)

Joint	DoF	Direction	Female Torque (N m)	Age (year)	Height (m)	Mass (kg)	Subject numbers	Ref.	Male Torque (N m)	Age (year)	Height (m)	Mass (kg)	Subject numbers	Ref.	β₁ (N m)	β₂ (N m)	β₃ (N m/year) Mean	Range	Ref	β₄ (N) Mean	Range	Ref	β₅ (N m/kg) Mean	Range	Ref
Wrist	WFE	+	15	25	1.68	59	78	[109]	25	24	1.79	74	90	[109]	−23.07	6.85	−0.04	−0.09 : 0.02	[109]	21.5	2.8 : 40.3	[109]	0.05	−0.08 : 0.18	[109]
		−	7	22	1.70	60	26	[112]	11	22	1.80	76	6	[112]	−31.67	1.05									
	WRUD	+	7	22	1.70	60	26	[112]	11	22	1.80	76	6	[112]	−31.67	1.05									
		−	8	22	1.70	60	26	[112]	12	22	1.80	76	6	[112]	−30.67	1.05									
Hip	HFE	+	126.1	22.2	1.70	67.3	10	[94]	148.5	26.2	1.79	85.1	10	[113]	−121.16	0.68	−0.92	−1.50 : −0.35	[109]	125	−91 : 298	[109]	0.82	−0.20 : 2.06	[109]
		−	205.4	22.2	1.70	67.3	10	[94]	182.4	26.2	1.79	85.1	10	[113]	−41.86	−44.68									
	HAA	+	131.6	20.1	1.61	57.2	44	[114]	202.5	25.5	1.80	75.0	80	[114]	−98.60	37.94									
		−	137.3	20.1	1.61	57.2	44	[114]	202.5	25.5	1.80	75.0	80	[114]	−92.88	32.22									
	HIER	+	32.1	24.4	1.70	68.4	15	[115]	37.4	25.8	1.79	81.3	15	[115]	−213.74	−15.42									
		−	25.3	24.4	1.70	68.4	15	[115]	45.5	25.8	1.79	81.3	15	[115]	−220.58	−0.44									
Knee	KFE	+	182.8	22.2	1.70	67.3	10	[94]	235.9	19.1	1.78	71.5	438	[116]	−12.13	37.84	−1.22	−1.88 : −0.73	[109]	89	−112 : 200	[109]	1.05	0.12 : 1.98	[109]
		−	104.1	22.2	1.70	67.3	10	[94]	158.5	19.1	1.78	71.5	438	[116]	−90.78	39.09									
Ankle	ADPF	+	33.0	22.2	1.70	67.3	10	[94]	36.2	19.1	1.78	71.5	438	[116]	−24.57	−0.21	−0.04	−0.17 : 0.05	[109]	14	−111 : 119	[109]	0.515	−0.05 : 1.08	[109]
		−	108.6	22.2	1.70	67.3	10	[94]	130.0	19.1	1.78	71.5	438	[116]	51.03	17.99									
	AEI	+	19.5	23.3	1.65	57.1	20	[117]	13.0	22.6	1.80	77.2	20	[118]	−32.07	−18.95									
		−	26.4	23.3	1.65	57.1	20	[117]	31.2	22.6	1.80	77.2	20	[118]	−25.17	−7.65									
	AAA	+	17.0	16.9	1.57	49.9	81	[119]	40.5	22.1	1.85	82.9	22	[120]	−30.04	2.83									
		−	14.0	16.9	1.57	49.9	81	[119]	34.9	22.1	1.85	82.9	22	[120]	−33.03	0.22									

Nomenclature

β_i	the anthropometric and torque measurements
Γ	the shape factor affecting the curvature of the torque-velocity hyperbola concentric relationship
F	the right-hand side of the dynamic equations, which consist of Coriolis, centrifugal, and gravitational effects
M	the mass matrix
Q	the external loads
μ	the maximum strength difference between dominant and non-dominant sides
ω	the joint's instantaneous angular speed
ρ	the impact of skin temperature
τ	the torque
τ_0	the peak isometric joint torque-producing capability
τ_ω	the active-torque-angular-speed-scaling function
τ_θ	the active-torque-position-scaling function
τ_{active}	the net active joint torque
τ_{pasive}	the passive joint torque
θ	the generalized coordinates
ς	the impact of exercise on maximum muscular strength
$_{GRW}$	the ground reaction wrench
$_{ISB}$	the International Society of Biomechanics (ISB) data
$_{Pelvis}$	the pelvis
$_{Raw}$	the raw data
a	the activation signal
c	the linear coefficient of rotational damping
d	the subject's dominant side constant
e	the subject's age
F	the force
h	the subject's height
k	the passive parameters identified from analyzing experimental data and fitting the nonlinear function
L	the segment length
M	the mass of each segment
m	the subject's body mass
n	the number of independent coordinates
N^J	the total number of joints
N^T	the total number of frames
o	the order of polynomial functions
P	the positions of anatomical landmarks
p	the 6 absolute coordinates for the pelvis with respect to ground
q	the coefficient of the polynomial
R	the maximum eccentric isokinetic torque
r	the scaling factors for the inertia matrix
S	the slope of eccentric to concentric phase transition
s	the subject's sex constant
T	the subject's skin temperature
t_{act}	the muscle activation time constants
t_{deact}	the muscle deactivation time constants
u	the excitation signal

v the number of human joints

w the subject's physical activity

Author contributions Conceptualization A.N. and J.M.; methodology, MapleSim software, MATLAB software, visualization, and writing the first draft A.N.; result evaluation A.N. and K.Z.; editing A.N., K.Z., and J.M.; funding acquisition J.M.; All authors have read and agreed to the published version of the manuscript.

Data Availability No datasets were generated or analysed during the current study.

Declarations

Competing interests The authors declare no competing interests.

References

1. Menache, A.: Understanding Motion Capture for Computer Animation, 2nd edn. Elsevier, Amsterdam (2010). https://doi.org/10.1016/C2009-0-62989-5
2. Mehta, D., Rhodin, H., Casas, D., Fua, P., Sotnychenko, O., Xu, W., Theobalt, C.: Monocular 3D human pose estimation in the wild using improved CNN supervision. In: Proceedings of the 2017 International Conference on 3D Vision, pp. 506–516. IEEE, Qingdao (2018). https://doi.org/10.1109/3DV.2017.00064
3. Pavlakos, G., Zhou, X., Derpanis, K.G., Daniilidis, K.: Coarse-to-fine volumetric prediction for single-image 3D human pose. In: Proceedings of the 30th IEEE Conference on Computer Vision and Pattern Recognition, pp. 1263–1272. IEEE, Honolulu (2017). https://doi.org/10.1109/CVPR.2017.139
4. Zhou, X., Huang, Q., Sun, X., Xue, X., Wei, Y.: Towards 3D human pose estimation in the wild: a weakly-supervised approach. In: Proceedings of the IEEE International Conference on Computer Vision, vol. 2017, pp. 398–407. IEEE, Venice (2017). https://doi.org/10.1109/ICCV.2017.51
5. Cai, Y., Ge, L., Liu, J., Cai, J., Cham, T.J., Yuan, J., Thalmann, N.M.: Exploiting spatial-temporal relationships for 3D pose estimation via graph convolutional networks. In: Proceedings of the IEEE International Conference on Computer Vision, vol. 2019, pp. 2272–2281. IEEE, Seoul (2019). https://doi.org/10.1109/ICCV.2019.00236
6. Pavllo, D., Feichtenhofer, C., Grangier, D., Auli, M.: 3D human pose estimation in video with temporal convolutions and semi-supervised training. In: Proceedings of the IEEE Computer Society Conference on Computer Vision and Pattern Recognition, vol. 2019, pp. 7745–7754. IEEE, Long Beach (2019). https://doi.org/10.1109/CVPR.2019.00794
7. Martinez, J., Hossain, R., Romero, J., Little, J.J.: A simple yet effective baseline for 3D human pose estimation. In: Proceedings of the IEEE International Conference on Computer Vision, vol. 2017, pp. 2659–2668. IEEE, Venice (2017). https://doi.org/10.1109/ICCV.2017.288
8. Kolotouros, N., Pavlakos, G., Black, M., Daniilidis, K.: Learning to reconstruct 3D human pose and shape via model-fitting in the loop. In: Proceedings of the IEEE International Conference on Computer Vision, vol. 2019, pp. 2252–2261. IEEE, Seoul (2019). https://doi.org/10.1109/ICCV.2019.00234
9. Kanazawa, A., Black, M.J., Jacobs, D.W., Malik, J.: End-to-end recovery of human shape and pose. In: Proceedings of the IEEE Computer Society Conference on Computer Vision and Pattern Recognition, pp. 7122–7131. IEEE, Salt Lake City (2018). https://doi.org/10.1109/CVPR.2018.00744
10. Loper, M., Mahmood, N., Romero, J., Pons-Moll, G., Black, M.J.: SMPL: a skinned multi-person linear model. Semin. Graph. Pap., Push. Bound. **2**, 851–866 (2023). https://doi.org/10.1145/3596711.3596800
11. Gartner, E., Andriluka, M., Coumans, E., Sminchisescu, C.: Differentiable dynamics for articulated 3D human motion reconstruction. In: Proceedings of the IEEE Computer Society Conference on Computer Vision and Pattern Recognition, vol. 2022, pp. 13180–13190. IEEE, New Orleans (2022). https://doi.org/10.1109/CVPR52688.2022.01284
12. Gartner, E., Andriluka, M., Xu, H., Sminchisescu, C.: Trajectory optimization for physics-based reconstruction of 3D human pose from monocular video. In: Proceedings of the IEEE Computer Society Conference on Computer Vision and Pattern Recognition, vol. 2022, pp. 13096–13105. IEEE, New Orleans (2022). https://doi.org/10.1109/CVPR52688.2022.01276

13. Shimada, S., Golyanik, V., Xu, W., Theobalt, C.: PhysCap: physically plausible monocular 3D motion capture in real time. ACM Trans. Graph. **39**(6), 1–16 (2020). https://doi.org/10.1145/3414685.3417877

14. Shimada, S., Golyanik, V., Xu, W., Pérez, P., Theobalt, C.: Neural monocular 3D human motion capture with physical awareness. ACM Trans. Graph. **40**(4), 1–15 (2021). https://doi.org/10.1145/3476576.3476640

15. Zell, P., Rosenhahn, B., Wandt, B.: Weakly-supervised learning of human dynamics. In: Lecture Notes in Computer Science (Including Subseries Lecture Notes in Artificial Intelligence and Lecture Notes in Bioinformatics), vol. 12371, pp. 68–84. Springer, Glasgow (2020). https://doi.org/10.1007/978-3-030-58574-7_5

16. Coumans, E., Bai, Y.: Pybullet, a python module for physics simulation for games, robotics and machine learning (2016). https://pybullet.org

17. Heiden, E., Millard, D., Coumans, E., Sheng, Y., Sukhatme, G.S.: NeuralSim: augmenting differentiable simulators with neural networks. In: Proceedings of the IEEE International Conference on Robotics and Automation, vol. 2021, pp. 9474–9481. IEEE, Xi'an (2021). https://doi.org/10.1109/ICRA48506.2021.9560935

18. Tripathi, S., Müller, L., Huang, C.-H.P., Taheri, O., Black, M.J., Tzionas, D.: 3D human pose estimation via intuitive physics. In: Proceedings of the IEEE Computer Society Conference on Computer Vision and Pattern Recognition, pp. 4713–4725. IEEE, Vancouver (2023). https://doi.org/10.1109/cvpr52729.2023.00457

19. Febrer-Nafría, M., Nasr, A., Ezati, M., Brown, P., Font-Llagunes, J.M., McPhee, J.: Predictive multi-body dynamic simulation of human neuromusculoskeletal systems: a review. Multibody Syst. Dyn. **58**, 1–41 (2022). https://doi.org/10.1007/s11044-022-09852-x

20. Ionescu, C., Papava, D., Olaru, V., Sminchisescu, C.: Human3.6M: large scale datasets and predictive methods for 3D human sensing in natural environments. IEEE Trans. Pattern Anal. Mach. Intell. **36**(7), 1325–1339 (2014). https://doi.org/10.1109/TPAMI.2013.248

21. Nasr, A.: Design, dynamics, and control of active-passive upper-limb exoskeleton robots. PhD thesis, University of Waterloo, Waterloo, ON, Canada (2022)

22. Dumas, R., Chèze, L., Verriest, J.P.: Body segment inertial parameters. J. Biomech. **40**(3), 543–553 (2007). https://doi.org/10.1016/j.jbiomech.2006.02.013

23. Wu, G., Siegler, S., Allard, P., Kirtley, C., Leardini, A., Rosenbaum, D., Whittle, M., D'Lima, D.D., Cristofolini, L., Witte, H., Schmid, O., Stokes, I.: ISB recommendation on definitions of joint coordinate system of various joints for the reporting of human joint motion – part I: ankle, hip, and spine. J. Biomech. **35**(4), 543–548 (2002). https://doi.org/10.1016/S0021-9290(01)00222-6

24. Nasr, A., Hashemi, A., McPhee, J.: Scalable musculoskeletal model for dynamic simulations of upper body movement. Comput. Methods Biomech. Biomed. Eng. **27**, 1–32 (2023). https://doi.org/10.1080/10255842.2023.2184747

25. Nasr, A., McPhee, J.: Scalable musculoskeletal model for dynamic simulations of lower body movement. Comput. Methods Biomech. Biomed. Eng., 1–27 (2024). https://doi.org/10.1080/10255842.2024.2316240

26. McConville, J.T., Churchill, T., Kaleps, I., Clauser, C.E., Cuzzi, J.: Anthropometric relationships of body and body segment moments of inertia. Tech. Rep., Air Force Aerospace Medical Research Laboratory, Aerospace Medical Division, Dayton, OH, USA (1980)

27. Durkin, J.L., Dowling, J.J.: Analysis of body segment parameter differences between four human populations and the estimation errors of four popular mathematical models. J. Biomech. Eng. **125**(4), 515–522 (2003). https://doi.org/10.1115/1.1590359

28. Pavol, M.J., Owings, T.M., Grabiner, M.D.: Body segment inertial parameter estimation for the general population of older adults. J. Biomech. **35**(5), 707–712 (2002). https://doi.org/10.1016/S0021-9290(01)00250-0

29. Robertson, D.G.E., Caldwell, G.E., Hamill, J., Kamen, G., Whittlesey, S.N.: Research Methods in Biomechanics, vol. 73603966. Human Kinetics, Inc. (2014). https://doi.org/10.5040/9781492595809

30. Norman-Gerum, V., McPhee, J.: Comprehensive description of sit-to-stand motions using force and angle data. J. Biomech. **112**, 110046 (2020). https://doi.org/10.1016/j.jbiomech.2020.110046

31. Banerjee, J.M., McPhee, J.: Symbolic sensitivity analysis of multibody systems. Comput. Methods Appl. Sci. **28**, 123–146 (2013). https://doi.org/10.1007/978-94-007-5404-1_6

32. Shah, H., Tripathi, S., Lee, L.F., Krovi, V.: Role of automated symbolic generation of equations of motion in mechanism and robotics education. In: Proceedings of the ASME Design Engineering Technical Conference, vol. 2, pp. 995–1002. ASME, Montreal (2010). https://doi.org/10.1115/DETC2010-28994

33. Anderson, D.E., Madigan, M.L., Nussbaum, M.A.: Maximum voluntary joint torque as a function of joint angle and angular velocity: model development and application to the lower limb. J. Biomech. **40**(14), 3105–3113 (2007). https://doi.org/10.1016/j.jbiomech.2007.03.022

34. Hoang, P.D., Gorman, R.B., Todd, G., Gandevia, S.C., Herbert, R.D.: A new method for measuring passive length-tension properties of human gastrocnemius muscle in vivo. J. Biomech. **38**(6), 1333–1341 (2005). https://doi.org/10.1016/j.jbiomech.2004.05.046

35. Yoon, Y.S., Mansour, J.M.: The passive elastic moment at the hip. J. Biomech. **15**(12), 905–910 (1982). https://doi.org/10.1016/0021-9290(82)90008-2

36. Yamaguchi, G.T.: Dynamic Modeling of Musculoskeletal Motion: A Vectorized Approach for Biomechanical Analysis in Three Dimensions, 1st edn. Springer, Boston (2006). https://doi.org/10.1007/978-0-387-28750-8

37. McNally, W., McPhee, J.: Dynamic Optimization of the Golf Swing Using a Six Degree-of-Freedom Biomechanical Model. Proceedings, vol. 2, pp. 243. MDPI, Brisbane (2018). https://doi.org/10.3390/proceedings2060243

38. Ezati, M., Ghannadi, B., McPhee, J.: A review of simulation methods for human movement dynamics with emphasis on gait. Multibody Syst. Dyn. **47**(3), 265–292 (2019). https://doi.org/10.1007/s11044-019-09685-1

39. Winters, J.M.: Hill-based muscle models: a systems engineering perspective. In: Multiple Muscle Systems, pp. 69–93. Springer, New York (1990). https://doi.org/10.1007/978-1-4613-9030-5_5. Chap. 5,

40. Inkol, K.A., Brown, C., McNally, W., Jansen, C., McPhee, J.: Muscle torque generators in multibody dynamic simulations of optimal sports performance. Multibody Syst. Dyn. **50**(4), 435–452 (2020). https://doi.org/10.1007/s11044-020-09747-9

41. Lewis, M.G., Yeadon, M.R., King, M.A.: The effect of accounting for biarticularity in hip flexor and hip extensor joint torque representations. Hum. Mov. Sci. **57**, 388–399 (2018). https://doi.org/10.1016/j.humov.2017.09.016

42. Millard, M., Emonds, A.L., Harant, M., Mombaur, K.D.: A reduced muscle model and planar musculoskeletal model fit for the simulation of whole-body movements. J. Biomech. **89**, 11–20 (2019). https://doi.org/10.1016/j.jbiomech.2019.04.004

43. Nasr, A., Dickerson, C.R., McPhee, J.: Experimental study of fully passive, fully active, and active–passive upper-limb exoskeleton efficiency: an assessment of lifting tasks. Sensors **24**(1), 63 (2023). https://doi.org/10.3390/s24010063

44. Nasr, A., Inkol, K.A., Bell, S., McPhee, J.: InverseMuscleNET: alternative machine learning solution to static optimization and inverse muscle modelling. Front. Comput. Neurosci. **15**, 759489 (2021). https://doi.org/10.3389/fncom.2021.759489

45. Lanshammar, K., Ribom, E.L.: Differences in muscle strength in dominant and non-dominant leg in females aged 20–39 years – a population-based study. Phys. Ther. Sport **12**(2), 76–79 (2011). https://doi.org/10.1016/j.ptsp.2010.10.004

46. Guette, M., Gondin, J., Martin, A.: Time-of-day effect on the torque and neuromuscular properties of dominant and non-dominant quadriceps femoris. Chronobiol. Int. **22**(3), 541–558 (2005). https://doi.org/10.1081/CBI-200062407

47. Gentil, P., Fischer, B., Martorelli, A.S., Lima, R.M., Bottaro, M.: Effects of equal-volume resistance training performed one or two times a week in upper body muscle size and strength of untrained young men. J. Sports Med. Phys. Fit. **55**(3), 144–149 (2015)

48. Ekblom, B., Bergh, U.: Influence of muscle temperature on maximal muscle strength and power output in human skeletal muscles. Acta Physiol. Scand. **107**, 33–37 (1979). https://doi.org/10.1111/j.1748-1716.1979.tb06439.x

49. Forrester, S.E., Yeadon, M.R., King, M.A., Pain, M.T.: Comparing different approaches for determining joint torque parameters from isovelocity dynamometer measurements. J. Biomech. **44**(5), 955–961 (2011). https://doi.org/10.1016/j.jbiomech.2010.11.024

50. Haering, D., Pontonnier, C., Bideau, N., Nicolas, G., Dumont, G.: Using torque–angle and torque–velocity models to characterize elbow mechanical function: modeling and applied aspects. J. Biomech. Eng. **141**(8), 084501 (2019). https://doi.org/10.1115/1.4043447

51. King, M.A., Wilson, C., Yeadon, M.R.: Evaluation of a torque-driven model of jumping for height. J. Appl. Biomech. **22**(4), 264–274 (2006). https://doi.org/10.1123/jab.22.4.264

52. Yeadon, M.R., King, M.A., Wilson, C.: Modelling the maximum voluntary joint torque/angular velocity relationship in human movement. J. Biomech. **39**(3), 476–482 (2006). https://doi.org/10.1016/j.jbiomech.2004.12.012

53. Alexander, R.M.: Optimum take-off techniques for high and long jumps. Philos. Trans. R. Soc. Lond. B, Biol. Sci. **329**(1252), 3–10 (1990). https://doi.org/10.1098/rstb.1990.0144

54. Dudley, G.A., Harris, R.T., Duvoisin, M.R., Hather, B.M., Buchanan, P.: Effect of voluntary vs. artificial activation on the relationship of muscle torque to speed. J. Appl. Physiol. **69**(6), 2215–2221 (1990). https://doi.org/10.1152/jappl.1990.69.6.2215

55. van Soest, A.J., Bobbert, M.F.: The contribution of muscle properties in the control of explosive movements. Biol. Cybern. **69**(3), 195–204 (1993). https://doi.org/10.1007/BF00198959

56. Sprigings, E.J.: Simulation of the force enhancement phenomenon in muscle. Comput. Biol. Med. **16**(6), 423–430 (1986). https://doi.org/10.1016/0010-4825(86)90066-1

57. Katz, B.: The relation between force and speed in muscular contraction. J. Physiol. **96**(1), 45–64 (1939). https://doi.org/10.1113/jphysiol.1939.sp003756

58. Brown, C., McNally, W., McPhee, J.: Optimal control of joint torques using direct collocation to maximize ball carry distance in a golf swing. Multibody Syst. Dyn. **50**(3), 323–333 (2020). https://doi.org/10.1007/s11044-020-09734-0

59. MacKenzie, S.J., Sprigings, E.J.: A three-dimensional forward dynamics model of the golf swing. Sports Eng. **11**(4), 165–175 (2009). https://doi.org/10.1007/s12283-009-0020-9

60. Romero, F., Alonso, F.J.: A comparison among different hill-type contraction dynamics formulations for muscle force estimation. Mech. Sci. **7**(1), 19–29 (2016). https://doi.org/10.5194/ms-7-19-2016

61. Buchanan, T.S., Lloyd, D.G., Manal, K., Besier, T.F.: Neuromusculoskeletal modeling: estimation of muscle forces and joint moments and movements from measurements of neural command. J. Appl. Biomech. **20**(4), 367–395 (2004). https://doi.org/10.1123/jab.20.4.367

62. Meyer, A.J.: Prediction of optimal rehabilitation outcomes post-stroke. PhD thesis, University of Florida, Gainesville, FL, USA (2016)

63. Rockenfeller, R., Günther, M., Schmitt, S., Götz, T.: Comparative sensitivity analysis of muscle activation dynamics. Comput. Math. Methods Med. **2015**, 1–16 (2015). https://doi.org/10.1155/2015/585409

64. Thelen, D.G.: Adjustment of muscle mechanics model parameters to simulate dynamic contractions in older adults. J. Biomech. Eng. **125**(1), 70–77 (2003). https://doi.org/10.1115/1.1531112

65. Yuan, Y., Wei, S.E., Simon, T., Kitani, K., Saragih, J.: SimPoE: simulated character control for 3D human pose estimation. In: Proceedings of the IEEE Computer Society Conference on Computer Vision and Pattern Recognition, pp. 7155–7165. IEEE, Nashville (2021). https://doi.org/10.1109/CVPR46437.2021.00708

66. Rempe, D., Guibas, L.J., Hertzmann, A., Russell, B., Villegas, R., Yang, J.: Contact and human dynamics from monocular video. In: Proceedings of the 19th ACM SIGGRAPH / Eurographics Symposium on Computer Animation, pp. 3–5. Springer, Glasgow (2020). https://doi.org/10.1007/978-3-030-58558-7_5

67. Kulig, K., Fietzer, A.L., Popovich, J.M.: Ground reaction forces and knee mechanics in the weight acceptance phase of a dance leap take-off and landing. J. Sports Sci. **29**(2), 125–131 (2011). https://doi.org/10.1080/02640414.2010.534807

68. Herzog, W., Nigg, B.M., Read, L.J., Olsson, E.: Asymmetries in ground reaction force patterns in normal human gait. Med. Sci. Sports Exerc. **21**(1), 110–114 (1989). https://doi.org/10.1249/00005768-198902000-00020

69. Castermans, T., Duvinage, M., Cheron, G., Dutoit, T.: Towards effective non-invasive brain-computer interfaces dedicated to gait rehabilitation systems. Brain Sci. **4**(1), 1–48 (2014). https://doi.org/10.3390/brainsci4010001

70. Wu, A.R., Dzeladini, F., Brug, T.J., Tamburella, F., Tagliamonte, N.L., Van Asseldonk, E.H., Van Der Kooij, H., Ijspeert, A.J.: An adaptive neuromuscular controller for assistive lower-limb exoskeletons: a preliminary study on subjects with spinal cord injury. Front. Neurorobot. **11**, 30 (2017). https://doi.org/10.3389/fnbot.2017.00030

71. Ivanenko, Y.P., Cappellini, G., Poppele, R.E., Lacquaniti, F.: Spatiotemporal organization of α-motoneuron activity in the human spinal cord during different gaits and gait transitions. Eur. J. Neurosci. **27**(12), 3351–3368 (2008). https://doi.org/10.1111/j.1460-9568.2008.06289.x

72. Wang, H., Basu, A., Durandau, G., Sartori, M.: Comprehensive kinetic and EMG dataset of daily locomotion with 6 types of sensors (2022). https://doi.org/10.5281/zenodo.6457662

73. Chiquier, M., Vondrick, C.: Muscles in action. In: Proceedings of the IEEE/CVF International Conference on Computer Vision, pp. 22034–22044. IEEE, Paris (2024). https://doi.org/10.1109/iccv51070.2023.02019

74. Nasr, A., Bell, S., He, J., Whittaker, R.L., Jiang, N., Dickerson, C.R., McPhee, J.: MuscleNET: mapping electromyography to kinematic and dynamic biomechanical variables. J. Neural Eng. **18**(4), 0460d3 (2021). https://doi.org/10.1088/1741-2552/ac1adc

75. Moromizato, K., Kimura, R., Fukase, H., Yamaguchi, K., Ishida, H.: Whole-body patterns of the range of joint motion in young adults: masculine type and feminine type. J. Physiol. Anthropol. **35**(1), 1–12 (2016). https://doi.org/10.1186/s40101-016-0112-8

76. Côté, J.N., Raymond, D., Mathieu, P.A., Feldman, A.G., Levin, M.F.: Differences in multi-joint kinematic patterns of repetitive hammering in healthy, fatigued and shoulder-injured individuals. Clin. Biomech. **20**(6), 581–590 (2005). https://doi.org/10.1016/j.clinbiomech.2005.02.012

77. Keller, T.S., Roy, A.L.: Posture-dependent isometric trunk extension and flexion strength in normal male and female subjects. J. Spinal Disord. Tech. **15**(4), 312–318 (2002). https://doi.org/10.1097/00024720-200208000-00009

78. Parijat, P., Lockhart, T.E., Liu, J.: EMG and kinematic responses to unexpected slips after slip training in virtual reality. IEEE Trans. Biomed. Eng. **62**(2), 593–599 (2015). https://doi.org/10.1109/TBME.2014.2361324

79. Bańkosz, Z., Winiarski, S.: Correlations between angular velocities in selected joints and velocity of table tennis racket during topspin forehand and backhand. J. Sports Sci. Med. **17**(2), 330–338 (2018)

80. Kumar, S.: Isolated planar trunk strengths measurement in normals: part III – results and database. Int. J. Ind. Ergon. **17**(2), 103–111 (1996). https://doi.org/10.1016/0169-8141(95)00042-9

81. Ferrario, V.F., Sforza, C., Serrao, G., Grassi, G.P., Mossi, E.: Active range of motion of the head and cervical spine: a three-dimensional investigation in healthy young adults. J. Orthop. Res. **20**(1), 122–129 (2002). https://doi.org/10.1016/S0736-0266(01)00079-1

82. Simoneau, M., Denninger, M., Hain, T.C.: Role of loading on head stability and effective neck stiffness and viscosity. J. Biomech. **41**(10), 2097–2103 (2008). https://doi.org/10.1016/j.jbiomech.2008.05.002

83. Jordan, A., Mehlsen, J., Bülow, P.M., Ostergaard, K., Danneskiold-Samsee, B.: Maximal isometric strength of the cervical musculature in 100 healthy volunteers. Spine **24**(13), 1343–1348 (1999). https://doi.org/10.1097/00007632-199907010-00012

84. Dvir, Z., Prushansky, T.: Reproducibility and instrument validity of a new ultrasonography-based system for measuring cervical spine kinematics. Clin. Biomech. **15**(9), 658–664 (2000). https://doi.org/10.1016/S0268-0033(00)00033-4

85. Doriot, N., Wang, X.: Effects of age and gender on maximum voluntary range of motion of the upper body joints. Ergonomics **49**(3), 269–281 (2006). https://doi.org/10.1080/00140130500489873

86. Engin, A.E., Kaleps, I.: Active muscle torques about long-bone axes of major human joints. Aviat. Space Environ. Med. **51**(6), 551–555 (1980)

87. Garner, B.A., Pandy, M.G.: Musculoskeletal model of the upper limb based on the visible human male dataset. Comput. Methods Biomech. Biomed. Eng. **4**(2), 93–126 (2001). https://doi.org/10.1080/10255840008908000

88. Soucie, J.M., Wang, C., Forsyth, A., Funk, S., Denny, M., Roach, K.E., Boone, D.: Range of motion measurements: reference values and a database for comparison studies. Haemophilia **17**(3), 500–507 (2011). https://doi.org/10.1111/j.1365-2516.2010.02399.x

89. Hutchins, E.L.: The musculoskeletal geometry of the human elbow and wrist: an analysis using torque–angle relationships. PhD thesis, University of Texas at Austin, Austin, TX, USA (1993)

90. Van Den Tillaar, R., Ettema, G.: A three-dimensional analysis of overarm throwing in experienced handball players. J. Appl. Biomech. **23**(1), 12–19 (2007). https://doi.org/10.1123/jab.23.1.12

91. Fu, W.Y., Cheng, G., Ma, Y.F., Yang, A.P.: Experimental research of range of motion about wrist joint. In: Proceedings of the International Conference on Digital Human Modeling and Applications in Health, Safety, Ergonomics and Risk Management, vol. 9745, pp. 3–12. Springer, Toronto (2016). https://doi.org/10.1007/978-3-319-40247-5_1

92. Delp, S.L., Grierson, A.E., Buchanan, T.S.: Maximum isometric moments generated by the wrist muscles in flexion–extension and radial–ulnar deviation. J. Biomech. **29**(10), 1371–1375 (1996). https://doi.org/10.1016/0021-9290(96)00029-2

93. Jessop, D.M., Pain, M.T.: Maximum velocities in flexion and extension actions for sport. J. Human Kinet. **50**(1), 37–44 (2016). https://doi.org/10.1515/hukin-2015-0139

94. Guilhem, G., Giroux, C., Couturier, A., Chollet, D., Rabita, G.: Mechanical and muscular coordination patterns during a high-level fencing assault. Med. Sci. Sports Exerc. **46**(2), 341–350 (2014). https://doi.org/10.1249/MSS.0b013e3182a6401b

95. Ibrahim, R., Kingma, I., de Boode, V., Faber, G.S., van Dieën, J.H.: Angular velocity, moment, and power analysis of the ankle, knee, and hip joints in the goalkeeper's diving save in football. Front. Sports Act. Living **2**, 13 (2020). https://doi.org/10.3389/fspor.2020.00013

96. Venter, M.R.M.R.: Physiological changes associated with lateral movement training of netball players. PhD thesis, Stellenbosch University, Stellenbosch, South Africa (2000)

97. Matsuda, Y., Kaneko, M., Sakurai, Y., Akashi, K., Yasuo, S.: Three-dimensional lower-limb kinematics during undulatory underwater swimming. Sports Biomech. (2021). https://doi.org/10.1080/14763141.2021.1995475

98. Lindsay, D.M., Maitland, M.E., Lowe, R.C., Kane, T.J.: Comparison of isokinetic internal and external hip rotation torques using different testing positions. J. Orthop. Sports Phys. Ther. **16**(1), 43–50 (1992). https://doi.org/10.2519/jospt.1992.16.1.43

99. Bayram, S., Kendirci, A.S.S., Kıral, D.D., Sahinkaya, T., Ekinci, M., Batıbay, S.G., Akgul, T., Sahinkaya, T., Ekinci, M., Batıbay, S.G., Akgul, T.: Isokinetic strength comparison of tuberosity fractures of the proximal fifth metatarsal treated with elastic bandage vs cast. Foot Ankle Int. **41**(6), 674–682 (2020). https://doi.org/10.1177/1071100720916429

100. Grimston, S.K., Nigg, B.M., Hanley, D.A., Engsberg, J.R.: Differences in ankle joint complex range of motion as a function of age. Foot Ankle Int. **14**(4), 215–222 (1993). https://doi.org/10.1177/107110079301400407

101. Zhang, S., Wortley, M., Chen, Q., Freedman, J.: Efficacy of an ankle brace with a subtalar locking system in inversion control in dynamic movements. J. Orthop. Sports Phys. Ther. **39**(12), 875–883 (2009). https://doi.org/10.2519/jospt.2009.3125

102. Czamara, A., Szuba, L., Krzeminska, A., Tomaszewski, W., Wilk-Franczuk, M., Szuba, L., Krzeminska, A., Tomaszewski, W., Wilk-Franczuk, M.: Effect of physiotherapy on the strength of tibial internal rotator muscles in males after anterior cruciate ligament reconstruction (ACLR). Med. Sci. Monit. **17**(9), CR523-531 (2011). https://doi.org/10.12659/MSM.881940

103. Yassierli, Nussbaum, M.A., Iridiastadi, H., Wojcik, L.A.: The influence of age on isometric endurance and fatigue is muscle dependent: a study of shoulder abduction and torso extension. Ergonomics **50**(1), 26–45 (2007). https://doi.org/10.1080/00140130600967323

104. Roberson, J.M., Witt, P., Gross, M.T.: A comparison of trunk extensor strength and squat lifting ability. J. Orthop. Sports Phys. Ther. **25**(2), 137–144 (1997). https://doi.org/10.2519/jospt.1997.25.2.137

105. Okada, T., Hakkaku, T., Iwai, K., Nakazato, K.: Weight category-dependent trunk muscle strength and its relation with LBP in elite judokas. Sports Med. Int. Open **05**(01), E14–E21 (2021). https://doi.org/10.1055/a-1303-2741

106. Vasavada, A.N., Li, S., Delp, S.L.: Three-dimensional isometric strength of neck muscles in humans. Spine **26**(17), 1904–1909 (2001). https://doi.org/10.1097/00007632-200109010-00018

107. Staudte, H.W., Duhr, N.: Age- and sex-dependent force-related function of the cervical spine. Eur. Spine J. **3**(3), 155–161 (1994). https://doi.org/10.1007/BF02190578

108. Hughes, R.E., Johnson, M.E., O'Driscoll, S.W., An, K.N.: Age-related changes in normal isometric shoulder strength. Am. J. Sports Med. **27**(5), 651–657 (1999). https://doi.org/10.1177/03635465990270051801

109. Harbo, T., Brincks, J., Andersen, H.: Maximal isokinetic and isometric muscle strength of major muscle groups related to age, body mass, height, and sex in 178 healthy subjects. Eur. J. Appl. Physiol. **112**(1), 267–275 (2012). https://doi.org/10.1007/s00421-011-1975-3

110. Frey-Law, L.A., Laake, A., Avin, K.G., Heitsman, J., Marler, T., Abdel-Malek, K.: Knee and elbow 3D strength surfaces: peak torque–angle–velocity relationships. J. Appl. Biomech. **28**(6), 726–737 (2012). https://doi.org/10.1123/jab.28.6.726

111. Kramer, J.F., Nusca, D., Bisbee, L., MacDermid, J., Kemp, D., Boley, S.: Forearm pronation and supination: reliability of absolute torques and nondorninant/dorninant ratios. J. Hand Ther. **7**(1), 15–20 (1994). https://doi.org/10.1016/S0894-1130(12)80036-6

112. Vanswearingen, J.M.: Measuring wrist muscle strength. J. Orthop. Sports Phys. Ther. **4**(4), 217–228 (1983). https://doi.org/10.2519/jospt.1983.4.4.217

113. Khalaf, K.A., Parnianpour, M., Karakostas, T.: Three dimensional surface representation of knee and hip joint torque capability. Biomed. Eng. Appl. Basis Commun. **13**(2), 53–65 (2001). https://doi.org/10.4015/S101623720100008X

114. Lopez-Valenciano, A., Ayala, F., De Ste Croix, M., Barbado, D., Vera-Garcia, F.J.: Different neuromuscular parameters influence dynamic balance in male and female football players. Knee Surg. Sports Traumatol. Arthrosc. **27**(3), 962–970 (2019). https://doi.org/10.1007/s00167-018-5088-y

115. Johnson, S., Hoffman, M.: Isometric hip-rotator torque production at varying degrees of hip flexion. J. Sport Rehabil. **19**(1), 12–20 (2010). https://doi.org/10.1123/jsr.19.1.12

116. Lategan, L.: Isokinetic norms for ankle, knee, shoulder and forearm muscles in young South African men. Isokinet. Exerc. Sci. **19**(1), 23–32 (2011). https://doi.org/10.3233/IES-2011-0392

117. Ottaviani, R.A., Ashton-Miller, J.A., Wojtys, E.M.: Inversion and eversion strengths in the weight-bearing ankle of young women. Am. J. Sports Med. **29**(2), 219–225 (2001). https://doi.org/10.1177/03635465010290021701

118. Ottaviani, R.A., Ashton-Miller, J.A., Kothari, S.U., Wojtys, E.M.: Basketball shoe height and the maximal muscular resistance to applied ankle inversion and eversion moments. Am. J. Sports Med. **23**(4), 418–423 (1995). https://doi.org/10.1177/036354659502300408

119. Kiriyama, S., Sato, H., Takahira, N.: Gender differences in rotation of the shank during single-legged drop landing and its relation to rotational muscle strength of the knee. Am. J. Sports Med. **37**(1), 168–174 (2009). https://doi.org/10.1177/0363546508324692

120. Stoffel, K.K., Nicholls, R.L., Winata, A.R., Dempsey, A.R., Boyle, J.J., Lloyd, D.G.: Effect of ankle taping on knee and ankle joint biomechanics in sporting tasks. Med. Sci. Sports Exerc. **42**(11), 2089–2097 (2010). https://doi.org/10.1249/MSS.0b013e3181de2e4f

Publisher's note Springer Nature remains neutral with regard to jurisdictional claims in published maps and institutional affiliations.